EXAMINING THE RELAXATION DYNAMICS OF INDOLE VIA IONIZATION AND FRAGMENTATION PUMP-PROBE SPECTROSCOPIES

by

TIMOTHY JUSTIN GODFREY

(Under the Direction of Susanne Ullrich)

ABSTRACT

Three pump-probe spectroscopic techniques are employed to investigate the involvement of the low-lying ^1L_a and ^1L_b states and the $^1\pi\sigma^*$ state in the deactivation process of indole following photoexcitation in the 201-282 nm range: (1) Time-resolved photoelectron spectroscopy, (2) hydrogen atom time-resolved kinetic energy release, and (3) time-resolved ion yield. Each method provides complementary information specific to the photophysical processes in indole, and a thorough examination of the excited states in the relaxation process is afforded.

INDEX WORDS: Indole, pump-probe spectroscopy, excited state, time resolved, relaxation dynamics, photophysics, eumelanin, photoelectron, kinetic energy release, ion yield

EXAMINING THE RELAXATION DYNAMICS OF INDOLE VIA IONIZATION AND FRAGMENTATION PUMP-PROBE SPECTROSCOPIES

by

TIMOTHY JUSTIN GODFREY

B.S., North Georgia College & State University, 2012

A Thesis Submitted to the Graduate Faculty of The University of Georgia in Partial Fulfillment of the Requirements for the Degree

MASTER OF SCIENCE

ATHENS, GEORGIA

2016

EXAMINING THE RELAXATION DYNAMICS OF INDOLE VIA IONIZATION AND FRAGMENTATION PUMP-PROBE SPECTROSCOPIES

by

TIMOTHY JUSTIN GODFREY

Major Professor: Susanne Ullrich

Committee: Henning Meyer
Uwe Happek

Electronic Version Approved:

Suzanne Barbour
Dean of the Graduate School
The University of Georgia
December 2016

DEDICATION

This work is dedicated to my mother and father, Tim and Nancy Godfrey, whose endless love and support of my academic endeavors made this possible.

ACKNOWLEDGEMENTS

This work was supported by the University of Georgia Provosts Faculty Research Grant and the National Science Foundation grant# NSF-CHE-0924456 and grant# NSF-CHE-1362237. The authors are also extremely grateful to Mr. D. R. Grimes and Mrs. Patricia Grimes for supporting this work through the Grimes Family Distinguished Graduate Fellowship Award and to Dr. Justin M. Turney for his help regarding theoretical aspects of the indole photophysics.

TABLE OF CONTENTS

Page

CHAPTER 1

INTRODUCTION

The efficacy of employing gas-phase, pump-probe techniques—like those utilized in these investigations—to explore the photophysics of biological molecules has been discussed extensively by Roberts and Stavros.[1] More specifically, these authors have reviewed in detail numerous gas-phase femtosecond studies of heteroaromatic biomolecules and their photoreactive subunits while delineating how the knowledge acquired from such research may extend to more complex molecules. In addition, several studies have successfully shown how gas-phase experiments help to elucidate the photodynamics of certain molecules in the condensed phase.[2-6] By exploiting this type of approach, Townsend *et al.*[7] have proposed investigating the so-called "building blocks" of the eumelanin polymer, which is the most abundant form of melanin in the human body, in an effort to better understand its response to absorption of ultraviolet (UV) radiation. Eumelanin, the structure of which is depicted in Figure 1.1, has three major constituents: 5,6-dihydroxyindole, indolequinone, and 5,6-dihydroxyindole-2-carboxylic acid.[8,9] As noted by Townsend *et al.*, a first approximation of the photophysics for each of these component molecules may be gleaned by studying the simpler compound indole, which is outlined in red in Figure 1.1 and will be the focus of this work.

Due to the large extent of theoretical calculations and experimental work available for indole, only a brief summary is provided here. To begin, we refer to the investigations by Sobolewski and Domcke[10] who employ several *ab initio* computational techniques to obtain potential energy profiles along the indole N-H stretch coordinate. These calculations unveil

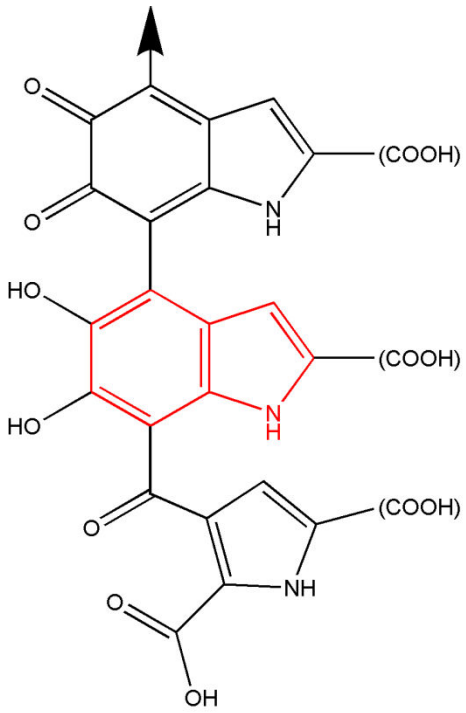

Figure 1.1 The structure of the eumelanin polymer is shown with the precursor indole outlined in red.

multiple conical intersections between the ground (S_0) and excited $^1\pi\pi^*$ and $^1\pi\sigma^*$ states, providing theoretical nonradiative relaxation pathways for photoexcited indole. In accordance with Platt's nomenclature,[11] the lower-lying states with $^1\pi\pi^*$ character will be referred to as ^1L_a and ^1L_b throughout the remainder of this work. Sobolewski and Domcke's multiconfigurational second-order perturbation theory (CASPT2) calculations predict the vertical excitation energies for the ^1L_b and ^1L_a states to be at 4.30 and 4.65 eV, respectively. Similar calculations reported by a number of other groups corroborate these results.[12-15] Sobolewski and Domcke also report calculations in a later study[16] that resulted in an upward shift of the same excitation energies—forming a near degeneracy between the $^1\pi\sigma^*$ state and the ^1L_a and ^1L_b states by essentially eliminating the large vertical gap between the $^1\pi\sigma^*$ and ^1L_a states illustrated in Figure 1.2(a). The authors briefly address the differences between their two studies by simply stating that CASPT2

generally underestimates excitation energies, while the coupled-cluster calculations employed in their latter study tend to overestimate the same values.

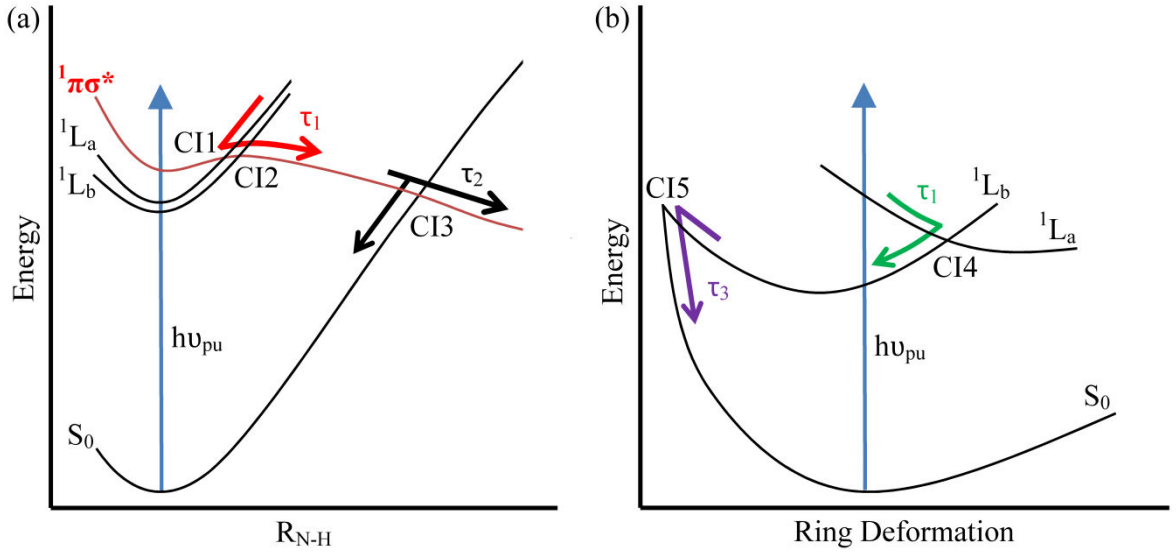

Figure 1.2 (a) Schematic of potential energy cuts along the N-H stretch coordinate according to the earlier work of Sobolewski and Domcke.[10] Conical intersections CI1, CI2, and CI3 between the $^1L_a/^1\pi\sigma^*$, $^1L_b/^1\pi\sigma^*$, and $^1\pi\sigma^*/S_0$ pathways are shown. (b) Schematic of the potential energy profiles along a generalized ring-deformation coordinate that preserves planarity of the indole molecule based on *ab initio* calculations by Giussani *et al.*[14] Conical intersections between the $^1L_a/^1L_b$ and $^1L_b/S_0$ pathways are labeled CI4 and CI5, respectively. Arrows and corresponding time constants describe individual relaxation steps: $^1L_a \rightarrow {}^1\pi\sigma^*$ and $^1L_a \rightarrow {}^1L_b$ (τ_1), $^1\pi\sigma^* \rightarrow S_0$ or N-H dissociation (τ_2), and $^1L_b \rightarrow S_0$ (τ_3). Figure reproduced with permission from J. Chem. Phys. **141**, 044314 (2014). Copyright 2014 AIP Publishing LLC.

Both theoretical[10] and experimental[17] investigations report relatively low oscillator strengths for the ^1L_b state (0.02 and 0.04, respectively) in comparison to the ^1L_a state (0.09 and 0.12, respectively). Nevertheless, the ^1L_b state has been inspected quite extensively and spectroscopic measurements have identified a number of vibronic bands[18-29] in the origin region (4.37 to ~4.58 eV), but the spectrum becomes increasingly featureless as the photoexcitation energy rises and the ^1L_a state is reached (around 4.54 eV).[30,31]

The quantum chemical calculations of Schmitt and co-workers[32] identify an additional deactivation pathway for photoexcited indole along ring-deformation coordinates. The results suggest that a conical intersection, which is located near the ^1L_a origin, between the ^1L_a and ^1L_b states may be accessed via Herzberg-Teller active modes; thus, an $^1L_a \rightarrow {}^1L_b$ transition is theoretically possible when considering ring puckering and in-plane distortions. Giussani *et al.*[14] obtain complementary results via minimum-energy-path calculations and also propose an $^1L_b/S_0$ conical intersection capable of mediating relaxation from the ^1L_b state back to the ground state. Figure 1.2(b) illustrates these additional relaxation pathways with CI4 and CI5 denoting the $^1L_a/^1L_b$ and $^1L_b/S_0$ conical intersections, respectively.

Due to its extremely low oscillator strength,[7,10] it is unlikely that the $^1\pi\sigma^*$ state is accessed directly through single-photon absorption. Therefore, it is deduced that population of this state occurs indirectly by way of internal conversion through $^1\pi\pi^*/^1\pi\sigma^*$ conical intersections.[33] The conical intersections that can lead to $^1\pi\sigma^*$ population from the ^1L_a and ^1L_b states are labeled CI1 and CI2 in Figure 1.2(a) with energetic onsets around 5 eV and 4.4 eV, respectively. The repulsive character of the $^1\pi\sigma^*$ state along the N-H coordinate[34] initiates movement toward the $^1\pi\sigma^*/S_0$ conical intersection, marked CI3 in Figure 1.2(a), providing two possible routes for deactivation: one leading to repopulation of the ground state and the other to H-atom generation. The latter process, as noted by Sobolewski and Domcke, transpires through direct N-H bond fission in the excited state. As indole relaxes toward the ground state via CI3, population of vibrationally excited indole molecules in the ground state provides an additional source for H-atom production via statistical unimolecular decay.[35] H-atoms generated from both processes are easily distinguished from one another based on their distinct kinetic energy distributions and appearance times. H-atoms associated with direct, excited-state N-H bond

dissociation maintain relatively high kinetic energies and fast rise times in comparison to H-atoms that slowly "boil off" the hot ground-state molecule.

Higher-lying $^1\pi\pi^*$ states, conventionally labeled ^1B_a and ^1B_b, have been investigated by Serrano-Andrés and Roos[12] and may be of relevance at the 201 nm photoexcitation wavelength employed in our investigations. The most apparent feature in their calculated spectrum is positioned at 5.84 eV, which is the same region where the strongest absorption peak for indole presents itself,[7,36-38] and is designated the ^1B_b-state vertical excitation energy. Serrano-Andrés and Roos also report the ^1B_a locale to be at approximately 6.44 eV. It should be noted that the adiabatic ionization potential for indole is located well above these $^1\pi\pi^*$ states at approximately 7.76 eV,[39-42] as is the vertical ionization potential at approximately 7.90 eV.[43-45]

Lin and co-workers[46] have inspected the photodissociation dynamics under collision-free conditions following excitation at 193 and 248 nm via multimass ion imaging techniques. Confirmation of two distinguishable H-atom contributions is gleaned and dissociation percentages from the electronically excited state are documented. At the 193 nm excitation wavelength, 54% of the indole molecule dissociates from the electronically excited state, yielding H-atoms with higher kinetic energies in comparison to H-atoms generated via alternative processes. Regarding the latter, the authors conclude that the residual indole dissociates indirectly via a hot ground state, complementing the previous discussion on the production of H-atoms with low kinetic energies.

Work by Ashfold *et al.*[47] employs high-resolution photofragment translational spectroscopy to investigate indole fragmentation dynamics. The authors identify "at least" three possible contributions to the observed H-atom yield, all of which are consistent with the previously discussed analyses regarding H-atom generation, following excitation at 193.3 nm

and a range of wavelengths between 240 and 286 nm. Their H-atom total kinetic energy release spectra reveal a bimodal distribution, and the authors conclude that the high-energy H-atoms are generated from the excited state via direct N-H bond fission along the $^1\pi\sigma^*$ state, while low-energy H-atoms are generated via statistical unimolecular decay of the vibrationally excited ground-state molecules and multiphoton processes. The work of Stavros *et al.*[35] expands upon and confirms this process by pumping indole molecules above the $^1\pi\pi^*/^1\pi\sigma^*$ conical intersections with 200 nm photons and observing the appearance of H-atoms with both high and low kinetic energies. In each case, H-atoms are generated on an ultrafast timescale (<200 fs), suggesting direct pathways for the generation of both H-atom distributions (the latter via multiphoton dissociative ionization rather than statistical unimolecular decay).

The aforementioned work by Townsend *et al.*[7] employs time-resolved photoelectron spectroscopy (TR-PES) techniques, with pump wavelengths centered at 249 and 273 nm, to procure information regarding the electronic relaxation dynamics of indole. In their study, it is deduced that the optically bright ^1L_a and ^1L_b electronic states and the spectroscopically dark $^1\pi\sigma^*$ state all contribute to the ultrafast relaxation process. At an excitation wavelength of 249 nm, the authors associate time constants of <100 fs, 0.7 ps, and 350 ps with decays along the ^1L_a, $^1\pi\sigma^*$, and ^1L_b states, respectively. This is in stark contrast with the spectroscopic work by Radloff and co-workers,[33] who measure only long-lived relaxation components at almost equivalent wavelengths, leading to the conclusion that no apparent coupling to the $^1\pi\sigma^*$ state takes place. Tentatively, Townsend *et al*. propose that the probing choices utilized in both investigations may cause the observed differences. Radloff and co-workers employ a 400 nm probe, requiring a multiphoton ionization scheme; whereas, Townsend *et al*. utilize a 300 nm probe, requiring only one photon to achieve ionization. The data presented by Glasser and Lami[48] also suggest a long-

lived component (~180 ps) exists at an excitation wavelength centered at 250 nm, which is nearly one half the 350 ps component acquired by Townsend *et al*., and no ultrafast component is reported. However, Glasser and Lami infer that N-H bond fission mediates the radiationless deactivation process from the ^1L_a state, an outcome now attributed to the $^1\pi\sigma^*$ state. Therefore, it is concluded by Townsend *et al*. that the initial excitation of the ^1L_a state decays nonadiabatically by way of populating either the long-lived ^1L_b state or the $^1\pi\sigma^*$ state.

Townsend *et al*.[7] also observe activity that they attribute to $^1\pi\sigma^*$-state dynamics at an excitation wavelength of 273 nm. This is highly corroborated by the author's theoretical investigations, as well as the latter calculations of Sobolewski and Domcke.[16] This wavelength, however, is notably longer than the onset of the $^1\pi\sigma^*$ channel previously reported by Ashfold *et al*. as 263 nm, thus clarification of this discrepancy necessitates additional experimental work. Nonetheless, according to the work by Townsend *et al.*, the $^1\pi\sigma^*$ state is actively participating in the indole relaxation process at the onset of the ^1L_a state (~273 nm), suggesting the $^1\pi\sigma^*$ onset is energetically lower than the ^1L_a state and/or some vibronic coupling between the two states exists.

Further inconsistencies in time constants emerge between the work of Townsend *et al*. and the time-resolved ion yield (TR-IY) investigations of Longarte and co-workers,[49] who report shorter relaxation times (~400 fs) for deactivation on the $^1\pi\sigma^*$ state at similar wavelengths. Although the experiments utilize disparate techniques, it is not unreasonable to suggest that the results should coincide more with one another. Longarte *et al*. report $^1\pi\sigma^*$-state dynamics at excitation wavelengths of 260, 248, and 243 nm with no apparent correlation between the extracted time constants and pump wavelengths. However, in agreement with Townsend *et al*., these authors also report substantially longer decay constants for relaxation on the ^1L_b state at

various wavelengths in comparison to the components associated with the ^1L_a and $^1\pi\sigma^*$ states. As the excitation energies increase, an apparent decrease in the $^1L_b \rightarrow S_0$ relaxation times is observed in both works.

To highlight the widespread disagreement among reported time constants, Table 1[50] provides a summary of the more recent decay times associated with ^1L_a-state (column 4), ^1L_b-state (column 5), and $^1\pi\sigma^*$-state (column 6) activity at various pump (column 2) and probe (column 3) wavelengths. The differing experimental techniques are also noted (column 1).

The work summarized in the following chapters assesses the relaxation dynamics of the indole molecule at excitation wavelengths centered at 201, 241, 250, 260, 270, 273, and 282 nm by employing three gas-phase spectroscopic techniques. The measurement of photoelectrons (TR-PES) affords direct observation of all existing relaxation pathways by probing the evolution of the excited states and disentangling their individual contributions by means of global analysis techniques. In contrast, detection of H-atoms (time-resolved kinetic energy release, TR-KER) eliminated along the indole N-H stretch coordinate is specific to the $^1\pi\sigma^*$ pathway and, as such, provides a second and independent analysis of its dynamics for comparison with TR-PES results. In addition, fragmentation pathways existing in the electronically excited states are readily observed via TR-IY experiments, effectively probing any dissociation paths that may emerge along a ring-deformation coordinate. The complementary information gleaned from each experimental technique in a single laboratory setting affords a more comprehensive examination of the lowest electronically excited states in the indole relaxation process. The work presented here thus contributes to a better overall understanding of the deactivation pathways and clarifies the $^1\pi\sigma^*$ dynamics at shorter excitation wavelengths as well as the energetic onset of $^1\pi\sigma^*$-state involvement in the indole deactivation process. The results also help to decipher the timescales

on which indole relaxation dynamics occur at all the aforementioned pump wavelengths. We also elaborate further on the suitability of different probe techniques for monitoring excited-state relaxation dynamics and propose an explanation for the inconsistent time constants found in the literature.

Table 1.1 The time constants presented here for the given pump (λ_{pu}) and probe (λ_{pr}) wavelengths are obtained using a variety of experimental techniques: time-resolved ion yield (TR-IY), time-resolved photoelectron spectroscopy (TR-PES), and, specific to H-atom photoproduct detection, time-resolved velocity map imaging (TR-VMI) and time-resolved kinetic energy release (TR-KER). Time constants obtained by our group are shown in bold. Table reproduced with permission from *Phys. Chem. Chem. Phys.*, 2015, **17**, 25197. Copyright 2015 the Owner Societies.

Technique	λ_{pu} (nm)	λ_{pr} (nm)	^1L_a	^1L_b	$^1\pi\sigma^*$
TR-VMI	200[i]	243.15	N/A	N/A	100 ± 30 fs
TR-PES	**201[ii]**	**294**	**<100 fs**	**23 ± 5 ps**	**405 ± 76 fs**
TR-KER	**201[ii]**	**243.15**	**N/A**	**N/A**	**367 ± 39 fs**
TR-IY	**201[ii]**	**294**	**<100 fs**	**23 ± 5 ps**	**385 ± 69 fs**
TR-IY	235[iii]	1305	-	150 ± 20 ps	-
TR-IY	239[iv]	394	-	>100 ps	-
TR-PES	**241**	**294**	**<100 fs**	**371 ± 85 ps**	**436 ± 157 fs**
TR-KER	**241**	**243.15**	**N/A**	**N/A**	**515 ± 63 fs**
TR-IY	243[iii]	1305	22 ± 9 fs	315 ± 50 ps	435 ± 125 fs
TR-IY	248[iii]	1305	22 ± 9 fs	ps	460 ± 145 fs
TR-PES	249[v]	300	<100 fs	350 ps (±20%)	700 fs (±20%)
TR-PES	**250**	**294**	**<100 fs**	**616 ± 64 ps**	**413 ± 144 fs**
TR-PES	250[iv]	400	-	>100 ps	-
TR-IY	250[iv]	400	-	>100 ps	-
TR-KER	**250**	**243.15**	**N/A**	**N/A**	**671 ± 84 fs**
TR-IY	255[iv]	310	-	>100 ps	-
TR-PES	**260**	**294**	**<100 fs**	**715 ± 98 ps**	**505 ± 100 fs**
TR-KER	**260**	**243.15**	**N/A**	**N/A**	**932 ± 91 fs**
TR-IY	260[iii]	1305	22 ± 9 fs	7 ± 2 ns	370 ± 110 fs
TR-PES	263[iv]	395	-	>100 ps	-
TR-IY	269[iii]	1305	39 ± 12 fs	ns	-
TR-PES	**270**	**294**	**272 ± 83 fs**	**ns**	**-**
TR-IY	272.5[iii]	1305	42 ± 9 fs	ns	-
TR-PES	**273**	**294**	**276 ± 142 fs**	**ns**	**-**
TR-PES	273[v]	300	<100 fs	∞	1200 fs (±20%)
TR-IY	278[iii]	1305	-	ns	-
TR-PES	**282**	**294**	**-**	**∞**	**-**

[i]Data from Ref. 35; [ii]Data from Ref. 63; [iii]Data from Ref. 49; [iv]Data from Ref. 33, this work does not distinguish between ^1L_a- and ^1L_b-state relaxation dynamics but instead associates the several hundred picoseconds time constant with relaxation from the initially prepared ππ* state(s)—assuming simultaneous excitation to both states; [v]Data from Ref. 7

CHAPTER 2

EXPERIMENTAL DETAILS

Pumping at 201 nm

The experimental apparatus (see Figure 2.1) contains a commercially available Coherent Inc. amplified femtosecond laser system (Legend Elite HE pumped with a Mira Model 900-F). The 800 nm fundamental output beam is used to generate both the pump and probe wavelengths via two tunable optical parametric amplifiers (OPAs). External mixing of 267 nm (~40 μJ/pulse), generated by way of a Coherent Inc. TOPAS-C, with the 800 nm fundamental (~500 μJ/pulse) in a type I barium borate (BBO) crystal produces the desired 201 nm (<7.0 μJ/pulse) pump wavelength. In all cases, probe beams are produced using a Coherent Inc. OPerA OPA.

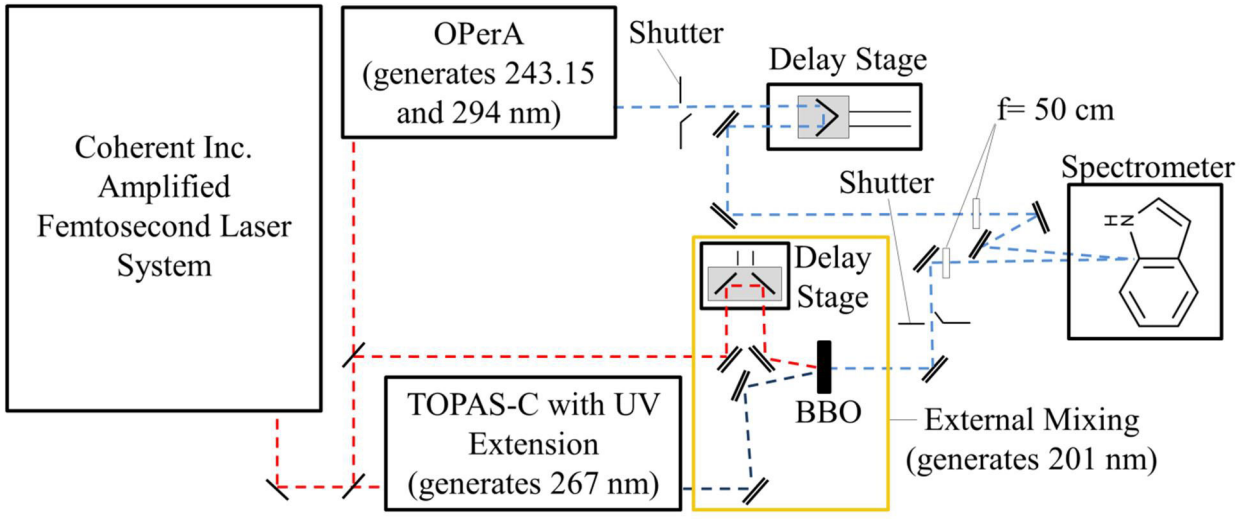

Figure 2.1 Schematic of the optical setup used to generate pump and probe pulses. Details regarding the magnetic bottle and TOF mass spectrometer are shown in Figure 2.2. Figure reproduced with permission from J. Chem. Phys. **141**, 044314 (2014). Copyright 2014 AIP Publishing LLC.

For TR-PES and TR-IY investigations, a 1 + 1' pump-probe scheme is preferred. To achieve this, the pump is maintained at a modest power to mitigate undesired multiphoton signals. The absorption spectra for the indole molecule[7,36-38] reveals minimal to no absorbance at 294 nm; hence, the probe is centered at this wavelength for TR-PES and TR-IY experiments to minimize probe-pump signals. For TR-KER measurements, which require ionization of neutral H-atoms, all probe powers are set higher (~7.0 μJ/pulse) to promote 2 + 1 resonance enhanced multiphoton ionization (REMPI) at 243.15 nm via the 2s state of neutral H-atoms.

A shutter system[51] is introduced to both the pump and probe beam paths (see Figure 2.1) for dynamic subtraction of undesired one-color, multiphoton signals. A motorized optical delay stage (Newport ILS150PP with ESP300 controller) facilitates scanning the relative timing of the pump and probe pulses. Both beams are combined at a small angle in a photoelectron photoion spectrometer, which affords kinetic energy measurements of photoelectrons and H-ions in a magnetic bottle (based on the principles outlined by Kruit and Read[52]) and parent/fragment ions in a linear time-of-flight (TOF) mass spectrometer (based on the Wiley-McLaren configuration[53]). The Gaussian cross-correlations are measured inside the spectrometer using a 50:50 mixture of 1,3-butadiene and helium as a calibration gas. Exact values are presented for each experimental setup in Chapter 3. Details regarding the custom-built measuring apparatuses[54] and the molecular-beam[55] machine are provided elsewhere and only described briefly here.

A schematic of the magnetic bottle and linear TOF spectrometer is shown in Figure 2.2. The magnetic bottle portion affords kinetic energy analysis through TOF measurements of both photoelectrons and photoionized H-atoms. Both the electrons and H-ions generated within the ionization region are exposed to a relatively strong, inhomogeneous magnetic field from a

permanent ring magnet, which is overlapped with a weak homogenous field generated by a solenoid, effectively steering their paths toward and through the flight tube to the microchannel plate detector (labeled Electron/H-atom Detector in Figure 2.2). The flight tube encompasses a

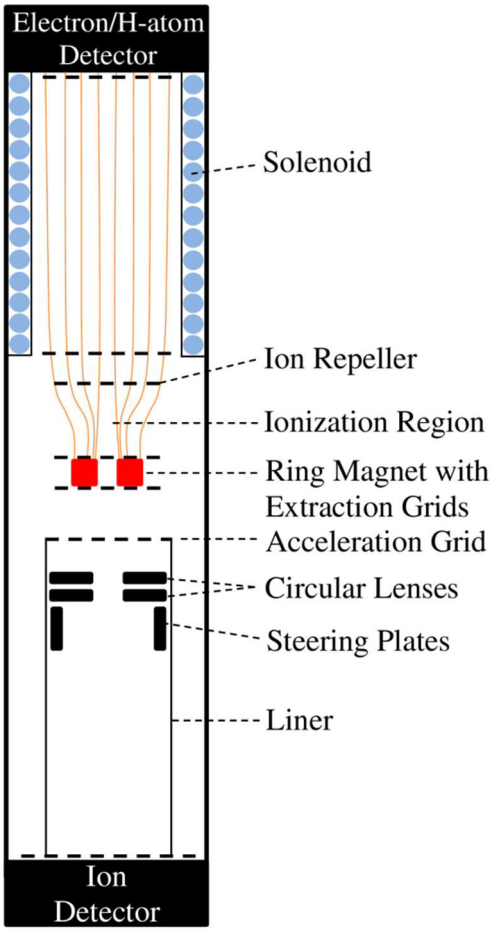

Figure 2.2. A schematic of the magnetic bottle and linear TOF spectrometer is shown. The various components are labeled and not drawn to scale. Figure reproduced with permission from J. Chem. Phys. **141**, 044314 (2014). Copyright 2014 AIP Publishing LLC.

region devoid of electrostatic fields. H-ion collection efficiency is increased by applying a repelling potential of +14 V to the extraction grids surrounding the ring magnet and the ion repeller. TOF to energy calibrations are performed using the procedure described in Ref. 54.

Larger photofragments generated in the ionization region are steered through the ring magnet and toward the TOF mass spectrometer by creating a potential difference of +1.5 kV between the ion repeller and the top extraction grid and -1.5 kV between the bottom extraction grid and acceleration grid. A series of circular lenses and steering plates are placed following the ring magnet for ion focusing and steering purposes. The flight tube is designed to produce a field-free region by means of a liner set to the acceleration grid potential. Ion flight times from the ionization region to the microchannel plate detector (labeled Ion Detector in Figure 2.2) are measured. TOF to mass conversion is performed using a 50:50 mixture of 1,3-butadiene/helium and a 50:50 combination of ammonia/helium as calibration gases.

Photoexcitation and ionization occurs via intersection of a focused pump/probe (f_{pu} = 50 cm/f_{pr} = 50 cm) pulse with a molecular beam initiated in a differentially pumped vacuum chamber that is attached to the spectrometer. The source oven is heated to 35 °C to ensure steady, yet sufficient, evaporation of the indole sample. The resulting indole vapor is routed to the spectrometer using helium as a carrier gas in a continuous expansion and is skimmed twice before reaching the ionization region.

Pumping in the 241-282 nm Range

The setup remains essentially the same for these investigations with only a few minor changes. In this case, all pump beams (241, 250, 260, 270, 273, and 282 nm) are generated using the Coherent Inc. OPerA OPA mentioned previously and span above and below the region where the $^1\pi\sigma^*$-state relaxation pathway becomes an energetically viable avenue for indole deactivation. The probe beams (294 nm for TR-PES and TR-IY; 243.15 nm for TR-KER) are generated with the Coherent Inc. TOPAS-C with UV extension mentioned in the previous section. Pump and probe beams are generated with pulse energies around 10 and 30 μJ/pulse,

respectively. Before intersecting the molecular beam, the pump pulse energy is reduced to a modest level (<1.7 μJ/pulse) and the probe to approximately 7.0 μJ/pulse for all TR-PES and TR-IY investigations. In regard to the TR-KER investigations, the probe beam pulse energy is set higher and centered around 243.15 nm to again promote H-atom detection. Scanning the relative pump-probe delay times is achieved with the same motorized delay stage (Newport ILS150PP with ESP300 controller) mentioned in the previous section but is positioned in the TOPAS-C beam path.

The same custom-built multipurpose spectrometer is utilized to record all measurements, and a 50:50 mixture of 1,3-butadiene and helium is used to find the Gaussian cross-correlation in each experiment: the results of which are reported in Chapter 4 in their respective sections. Photoelectron energy spectra are calibrated with the same butadiene-helium mixture and a 50:50 mixture of ammonia and helium using the photoelectron spectra in Refs. 56 and 57, respectively.

CHAPTER 3

PUMPING INDOLE AT 201 NM

To aid in the following discussion, the reader is referred to the schematics in Figure 1.2, which present an illustration of the relaxation pathways and nomenclature of associated time constants used throughout this work. The dynamics associated with $^1L_a \rightarrow {}^1L_b$ and $^1L_a \rightarrow {}^1\pi\sigma^*$ transitions occur simultaneously and on timescales that are not discernable in our experiments, hence a single time constant τ_1 is assigned. The time constant τ_2 corresponds to $^1\pi\sigma^*$ deactivation via $^1\pi\sigma^* \rightarrow S_0$ internal conversion or H-atom dissociation along the N-H coordinate, whereas τ_3 describes the $^1L_b \rightarrow S_0$ transition.

It is also worth noting that a single photon at 201 nm (6.17 eV) pumps the indole molecule well above the ^1L_a-state origin. The authors are aware that this excess energy could very likely place the molecule in another state with $^1\pi\pi^*$ character, traditionally labeled ^1B_b.[11] However, if this is the case, our results discussed in detail below indicate that a ^1B_b-state to ^1L_a-state relaxation occurs on timescales well below our time resolution. For this reason, the discussion below focuses on the dynamics originating from the ^1L_a state.

Time-Resolved Photoelectron Spectroscopy

The results herein utilize a pump wavelength centered at 201 nm and a probe wavelength centered at 294 nm with a Gaussian cross-correlation of 173 ± 20 fs as measured inside the magnetic bottle spectrometer. A color map of the TR-PES spectrum is presented in Figure 3.1 as

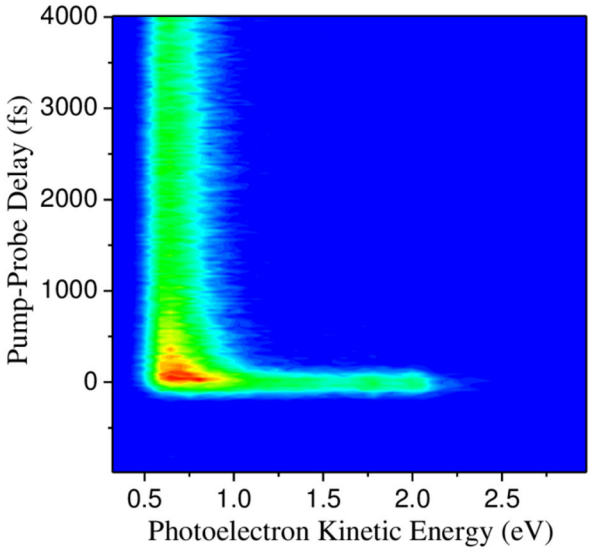

Figure 3.1 Experimental TR-PES spectrum of indole photoexcited at 201 nm is presented here in the form of a two-dimensional color map. Figure reproduced with permission from J. Chem. Phys. **141**, 044314 (2014). Copyright 2014 AIP Publishing LLC.

a function of the measured photoelectron kinetic energies and pump-probe delays. It contains three distinguishable regions: The first displaying a relatively long-lived signal between 0 and ~1 eV; however, a second and faster decaying signal partially overlaps with this region at ~0.9 eV. A third and short-lived signal is apparent between 1.25 and 2.25 eV, where some overlap with the other two components is likely. These contributions to the overall TR-PES spectrum are deconvoluted using a global analysis program based on a Levenberg-Marquardt optimization algorithm, which simultaneously fits spectra and extracts time constants of individual channels. A fourth channel with a negative decay constant of ~-60 fs is needed to account for a small, but nonzero, probe-pump signal from unintended, yet unavoidable, multiphoton processes. This channel is unrelated to the excited-state dynamics of interest and not discussed further. The fit results of the three pump-probe channels are presented as color maps in Figure 3.2. Electron

binding energies are readily calculated by subtracting the measured photoelectron kinetic energy from the total photon energy of approximately 10.4 eV.

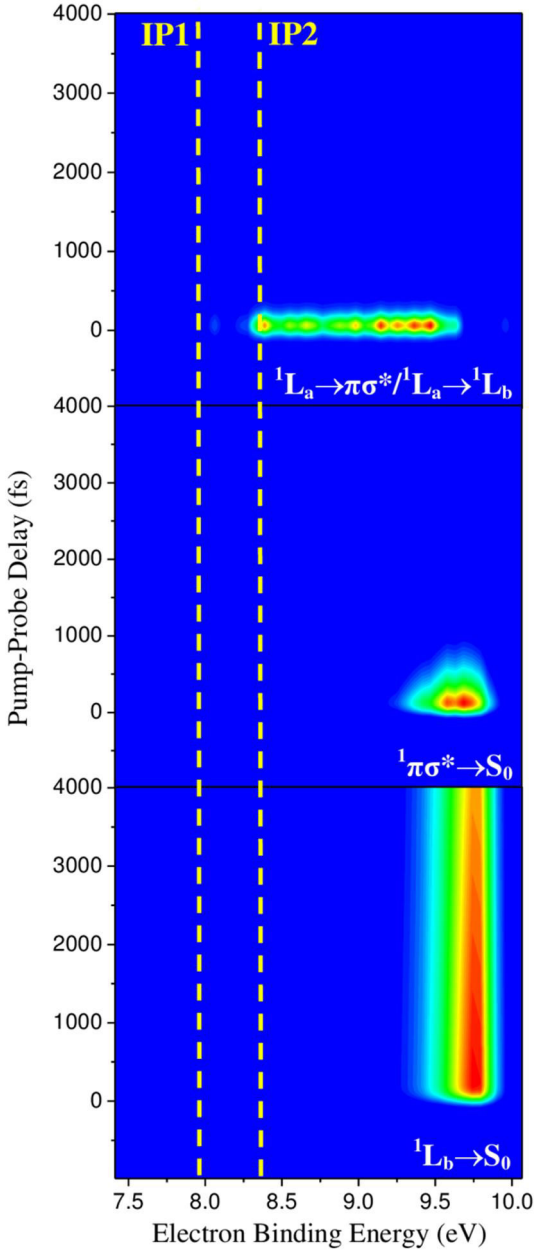

Figure 3.2 Color maps are presented for each individual channel obtained through the global analysis of the TR-PES data. The measured electron kinetic energies are transformed to electron binding energies for comparison to the known indole ionization potentials (yellow-dashed lines labeled IP1 and IP2). Figure reproduced with permission from J. Chem. Phys. **141**, 044314 (2014). Copyright 2014 AIP Publishing LLC.

The appearance of a long-lived channel prompted a separate scan (not presented here) extending to a delay time of approximately 300 ps beyond time-zero (*i.e.*, zero pump-probe delay) to extract a reliable decay constant (23 ± 5 ps) associated with this signal, which is then fixed in the global analysis of the short-range scan. The time traces and decay associated spectra for the individual channels are presented in Figures 3.3(a) and 3.3(b), respectively.

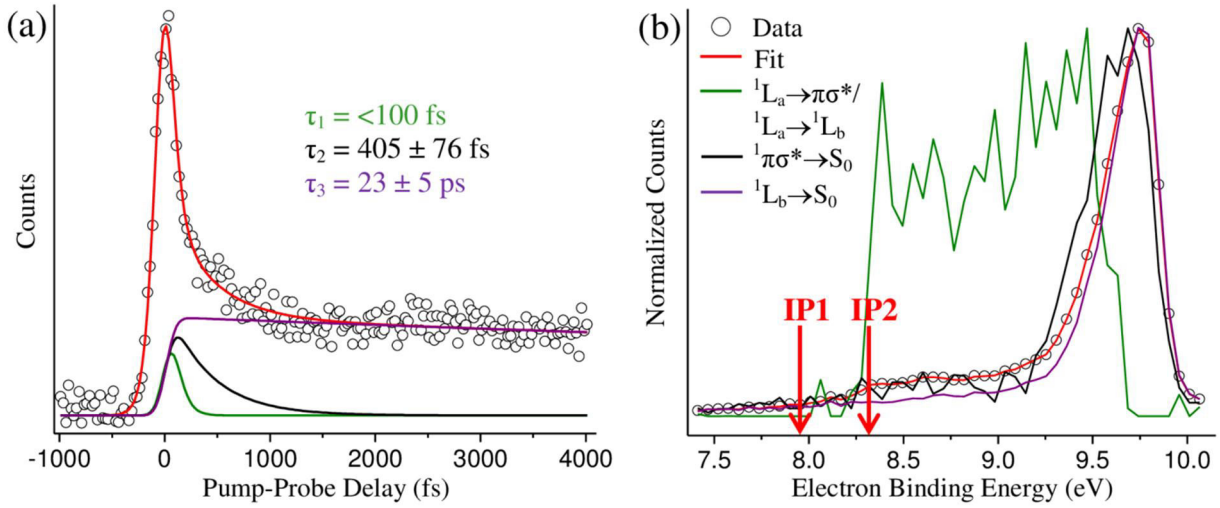

Figure 3.3 TR-PES signal (○), fit (red) and individual contributions (green, black, and purple) integrated over all photoelectron kinetic energies are shown in (a) with the corresponding photoelectron spectrum (○), fit (red) and decay associated spectra (green, black, and purple) portrayed in (b). The first and second vertical ionization potentials (IP1 and IP2, respectively) for the indole molecule are marked in (b). The respective values are 7.90 and 8.35 eV. Figure reproduced with permission from J. Chem. Phys. **141**, 044314 (2014). Copyright 2014 AIP Publishing LLC.

Further analysis and interpretation of the photoelectron spectra is based on ionization correlations. The first two vertical ionization potentials, both associated with removal of an electron from a π orbital, are reported by Eland as 7.90 and 8.35 eV[44] and are labeled as IP1 and IP2, respectively, in both Figures 3.2 and 3.3(b). Eland reports 8.35 eV as a "doubtful" value; however, other works report similar results.[43,45] Founded on orbital computations, Townsend *et al*. link the ^1L_a state to a transition originating from the highest occupied molecular orbital (HOMO), while the ^1L_b and $^1\pi\sigma^*$ transitions originate from the HOMO-1.[7] Thus, they expect that

the ^1L_a state preferentially ionizes to the D_0 (IP1) state, while the ^1L_b state ionizes into the D_1 (IP2) state. However, due to the pump-photon energy of 6.17 eV, the electronically excited ^1L_a and ^1L_b states are vibrationally excited by 1.5 eV and 1.8 eV, respectively, and the maximum photoelectron signals are expected to be shifted correspondingly with respect to IP1 and IP2, which is observed here.

Based on the observation of only one ultrafast decay constant, it is concluded here that $^1L_a \rightarrow {}^1L_b$ and $^1L_a \rightarrow {}^1\pi\sigma^*$ relaxations transpire on timescales <100 fs, further ascertaining the previous works outlined in Chapter 1. This particular time constant is extracted from the green delay trace displayed in Figure 3.3(a).

A second component arises, shown in Figure 3.3(a) as a black delay trace, from the global analysis with an associated decay time of 405 ± 76 fs. We relate this component to activity mediated by the $^1\pi\sigma^*$ relaxation pathway. As previously mentioned, Longarte *et al.*[49] report a relaxation time correlated with $^1\pi\sigma^*$ activity of approximately 400 fs for excitation wavelengths centered at 260, 248, and 243 nm, with no apparent trend between excitation wavelength and the extracted time constants. This bolsters confidence in this investigation's extracted value at a much shorter excitation wavelength. However, there is disagreement with Townsend *et al.*, who measure a $^1\pi\sigma^*$ lifetime nearly twice as long following 249 nm photoexcitation. On the other hand, an increase in lifetime to 1.2 ps at 273 nm, as observed by Townsend *et al.*, can be expected since significantly less energy is available to surmount the barrier along the $^1\pi\sigma^*$ pathway.

The time constant extracted from the long-range scan, τ_3 = 23 ± 5 ps, conforms to the trend observed by Longarte *et al.* that a decrease in excitation wavelength results in a shorter ^1L_b-state lifetime (*i.e.*, nanoseconds at 273 nm, 315 ps at 243 nm, and 115 ps at 235 nm).[49] The

authors explain this trend based on triplet-triplet energy transfer experiments implemented by Sukhodola,[58] which demonstrate a quantum yield drop with an increase in excitation energy—a direct consequence of an increase in the internal quantum yield to the ground state. Extrapolating from work on the photophysical properties of aniline[59] and 1-Aminonaphthalene,[60] it is viable that the relaxation rate of indole from the ^1L_b state may also increase due to the accessibility of additional conical intersections at higher excitation energies. In any case, our results exhibit a continuation of this trend at 201 nm, alluding to similar photophysical processes within the indole molecule as those found at longer wavelengths.

Time-Resolved Kinetic Energy Release

The TR-KER spectra presented here are obtained with a pump beam centered at 201 nm and probe beam at 243.15 nm. The Gaussian cross-correlation measured inside the spectrometer is approximately 288 ± 20 fs. The H-atom kinetic energy spectrum of the final steady-state distribution is displayed in Figure 3.4. The red-dotted lines partition the graph into three regions. Region III is simply the baseline signal, while regions I and II clearly enclose two distinct contributions to the bimodal H-atom kinetic energy distribution located at approximately 0.22 eV and 0.85 eV, respectively. Delay traces corresponding to regions I and II are shown in Figure 3.5. The signal in region II is integrated from 0.60 to 1.67 eV to obtain the delay trace shown in Figure 3.5(a) and is fitted with a Gaussian convoluted single-step function to extract the rise time of this particular H-atom signal. The signal in region I is integrated from 0 to 0.60 eV to produce the delay trace in Figure 3.5(b), which resembles a Gaussian convoluted double-step function.

It is known that H-atoms may fissure from an N-H bond as a molecule relaxes along a $^1\pi\sigma^*$ relaxation pathway,[61] and the appearance of two separate peaks in the H-atom kinetic energy spectrum provides a means of distinguishing H-atoms generated via $^1\pi\sigma^*$-state activity

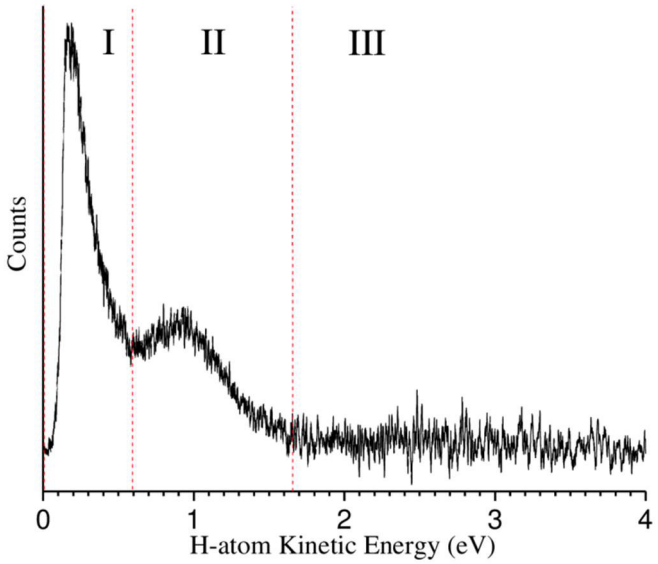

Figure 3.4. The steady-state H-atom kinetic energy spectrum of indole photodissociated at 201 nm is presented here. Region I encompasses signal associated with low-energy H-atoms. Region II corresponds to H-atoms with high kinetic energies (*i.e.*, H-atoms formed via dissociation along the $^1\pi\sigma^*$ relaxation pathway). Region III is simply the baseline signal. The red-dotted lines show the chosen gates for the delay traces presented in Figure 3.5. Figure reproduced with permission from J. Chem. Phys. **141**, 044314 (2014). Copyright 2014 AIP Publishing LLC.

from H-atoms that appear from multiphoton dissociative processes and statistical unimolecular decay. As discussed in Chapter 1, the kinetic energies associated with these additional, unwanted processes should be lower (*i.e.*, the signal that appears in region I) than those that appear via dissociation along a $^1\pi\sigma^*$ pathway (*i.e.*, the signal that appears in region II). The peaks are also consistent with the high-resolution total kinetic energy release spectra acquired by Ashfold *et al.*,[47] where two distinct H-atom peaks are reported at 1800 cm^{-1} (0.22 eV) and 6800 cm^{-1} (0.84 eV), respectively. Because the mass of the H-atom is much smaller than that of the indolyl (*i.e.*, indole less one H-atom) cofragment, the recoil can be neglected and this close similarity between the H-atom kinetic energy spectrum and the total kinetic energy spectra is expected. Therefore,

these results confirm the formation of H-atoms with both high and low kinetic energies following excitation at 201 nm.

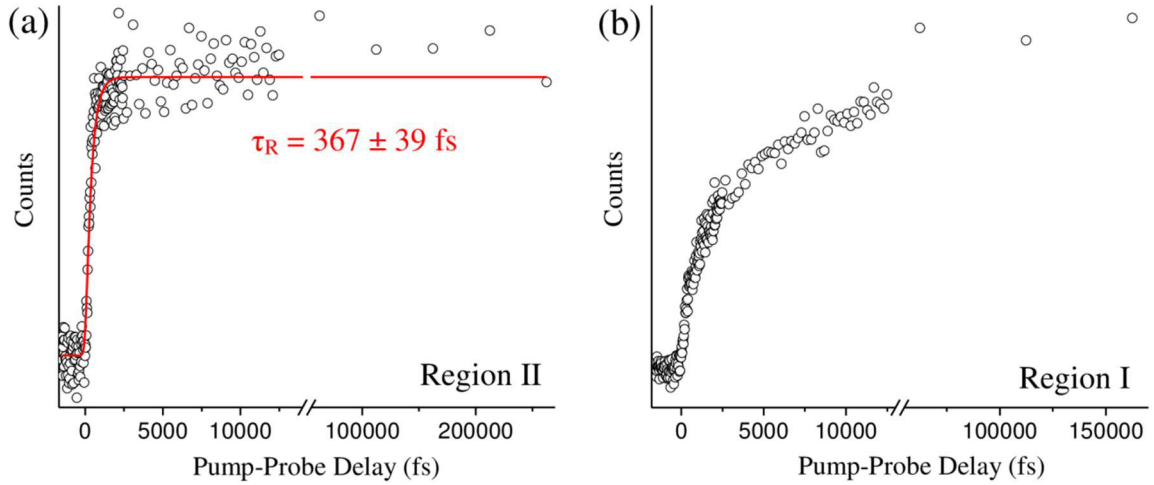

Figure 3.5 Delay traces obtained from the TR-KER measurements shown in Figure 3.4 are presented here. The traces correspond to the generation of (a) high kinetic energy H-atoms and (b) low kinetic energy H-atoms. Figure reproduced with permission from J. Chem. Phys. **141**, 044314 (2014). Copyright 2014 AIP Publishing LLC.

The extracted rise time for the appearance of H-atoms with high kinetic energies in region II is determined to be 367 ± 39 fs. This is slightly less than the 405 ± 76 fs component extracted from our TR-PES investigations, but the values agree within the reported error. The shorter time constant could be a direct effect of the imbricated H-atom signal associated with multiphoton dissociative ionization and statistical unimolecular decay (region I) with that attributed to a $^1\pi\sigma^*$ relaxation pathway (region II). Stavros and Iqbal[35] conduct similar investigations but report a time constant nearly four times shorter. The reason for this discrepancy is unclear; however, our result is highly supported by the previously discussed TR-PES and the following TR-IY scans and is consistent with the $^1\pi\sigma^*$ time constants obtained by Longarte *et al*.[49] at longer wavelengths.

The overall structure of the delay trace extracted from region I clearly differs in comparison to the results of Stavros and Iqbal, albeit excitation takes place at almost equivalent

wavelengths. The reason for the dissimilarity is not evident; however, the continuous rise observed in Figure 3.5(b) is highly reproducible and equally as conspicuous in separate scans (not presented here) extending only 4 ps beyond zero pump-probe delay. The trace appears to have two major contributions: One component arising on an ultrafast timescale (<200 fs) and another at a much slower rate (picosecond-nanosecond range). A fast component observed within this low kinetic energy region suggests that a direct pathway to H-atom generation, as suggested by Stavros and Iqbal, is feasible and likely attributed to multiphoton processes. Statistical decay of the hot molecule following internal conversion to the ground state (S_0) is attributed to the longer rise; however, additional experiments are needed to fully explicate the dynamics within this region. Because this work aims to assess the high-energy H-atoms, dynamics within region I are not discussed further.

Time-Resolved Ion Yield

A time-resolved time-of-flight mass spectrum is recorded following excitation at 201 nm with a 294 nm probe. The Gaussian cross-correlation measured in the spectrometer for this investigation is approximately 245 ± 20 fs. Figure 3.6 shows the mass spectrum, integrated over all pump-probe delays, with the region between mass/z = 20 and 70 enlarged within the inset for clarity. The most intense peak at 117 is associated with the indole parent ion, while the smaller fragment peaks arise at the mass-to-charge ratio (mass/z) values 90, 89, 60-65, 51, 39, and 26-28 and, upon closer inspection, peaks also form at 116 and 118. Fragmentation mechanics from the parent molecule remain unclear; however, the aforementioned work by Ashfold *et al.*[47] assesses the fragmentation process—associating the peaks at mass/z = 90 and 89 with the $C_7H_6^+$ and $C_7H_5^+$ fragment ions, respectively. The work by Lin *et al.*[46] suggest that these two fragments emerge following ionization of the excited indole molecule, and, in conjunction with mass

spectra obtained via electron impact ionization (*i.e.*, no involvement from the excited state),[62] it appears that all fragment peaks in the mass spectrum result from activity in the ionic state. As such, the results presented here indicate that no additional fragmentation pathways exist in the neutral electronically excited states except N-H dissociation along the $^1\pi\sigma^*$ path, which is demonstrated in the TR-KER experiments discussed previously. More specifically, it is concluded that evolution on the ^1L_b state along ring-deformation coordinates yields repopulation of the neutral ground state (S_0). Nevertheless, the smaller fragments are not absent of information useful to this discussion as their decay times should be directly correlated to activity within the parent molecule.

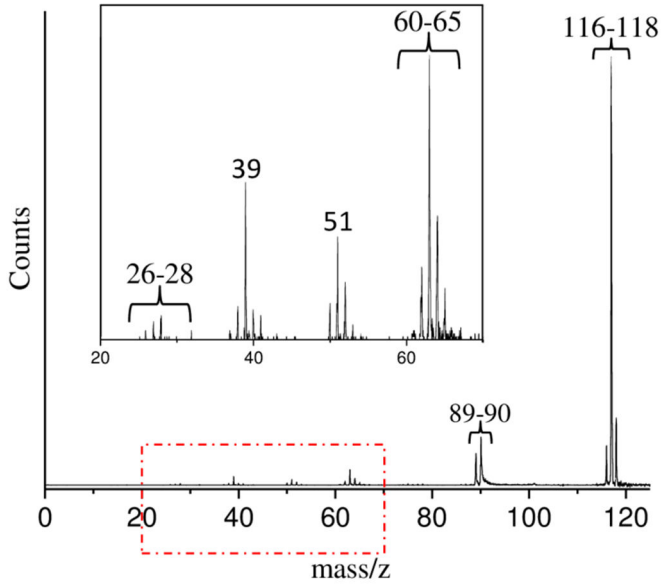

Figure 3.6 The TOF mass spectrum for the indole molecule following excitation at 201 nm is shown. Distinguishable peaks emerge at mass/z = 118, 117, 116, 90, and 89. The region outlined in red is enlarged in the inset to clarify the appearance of smaller fragments at mass/z = 60-65, 51, 39, and 26-28. Figure reproduced with permission from J. Chem. Phys. **141**, 044314 (2014). Copyright 2014 AIP Publishing LLC.

The discussion will begin with the dynamics observed in the parent ion at mass/z = 117. This and the other prominent peaks in the mass spectrum, which are labeled in Figure 3.6, are analyzed for their time dependence. Save for the peak at mass/z = 116, all delay traces are best described by a Gaussian convoluted triple exponential decay function. As in the short-range TR-PES investigation, the time constant corresponding to ^1L_b-state activity is fixed in this analysis at 23 ± 5 ps. The resulting delay trace, exponential decay components, and extracted time parameters associated with the parent ion are displayed in Figure 3.7. It is deduced that transition

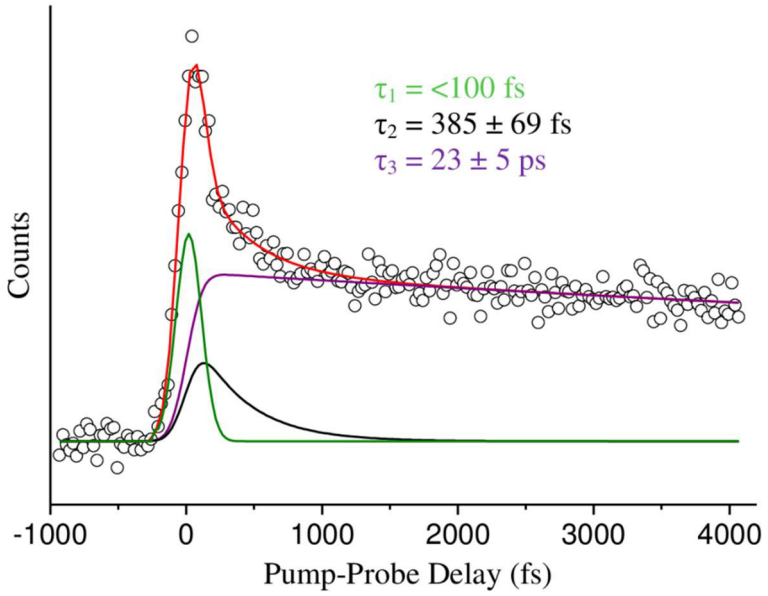

Figure 3.7 The overall delay trace (○), best-fit trendline (red), individual components, and extracted time constants associated with the TR-IY of the parent ion (mass/z = 117 in Figure 3.6) are shown. The delay trace in green correlates with $^1L_a \rightarrow {}^1L_b$ and $^1L_a \rightarrow {}^1\pi\sigma^*$ transitions. The black delay trace corresponds to $^1\pi\sigma^* \rightarrow S_0$ relaxation and the purple delay trace represents $^1L_b \rightarrow S_0$ internal conversion. Figure reproduced with permission from J. Chem. Phys. **141**, 044314 (2014). Copyright 2014 AIP Publishing LLC.

from the excited ^1L_a state to the lower-lying ^1L_b and $^1\pi\sigma^*$ states transpires on an ultrafast timescale (<100 fs). The component associated with $^1\pi\sigma^*$ relaxation is determined to be 385 ± 69 fs. This is within one standard deviation of the values obtained via TR-PES and TR-KER;

therefore, these results extracted from TR-IY highly corroborate those reported in the previous sections.

Time traces associated with the most prominent fragment peaks less than mass/z = 116 are fitted with the same triple-decay function, and signals are described well with the three aforementioned lifetimes garnered from the parent molecule. The similarity in dynamics supports the aforementioned conclusion that the fragments result from dissociative ionization rather than photodissociation of a neutral excited state along a ring-deformation pathway.

The peak arising at mass/z = 116 is associated with the indolyl radical, thus its appearance time is expected to be closely correlated to $^1\pi\sigma^*$-state activity. To assess this conjecture, the delay trace associated with this peak is fitted with a Gaussian convoluted double exponential decay function combined with a Gaussian convoluted single-step function, allowing derivation of a rise time, τ_R, for the indolyl radical. Inclusion of the double-decay term in the fitting function is required to account for signal contributions in the mass channel from dissociative ionization of the parent molecule while evolving along $^1L_a \rightarrow {}^1\pi\sigma^*$ and $^1\pi\sigma^* \rightarrow S_0$ pathways. The time constants from the TR-PES study are fixed in the double-decay term throughout this analysis. A third exponential decay is not necessary to adequately describe the time trace; hence, it is deduced that dissociative ionization of the ^1L_b state does not lead to H-atom extraction. Individual fit contributions and the rise time associated with the peak at mass/z = 116 is portrayed in Figure 3.8. A rise time of 427 ± 76 fs is attained, and the authors predominantly associate this rise, or appearance of the indolyl radical, to dissociation along the N-H coordinate via the $^1\pi\sigma^*$ relaxation pathway. Overall, the TR-IY study yields results that strongly avouch the TR-PES time constants discussed previously.

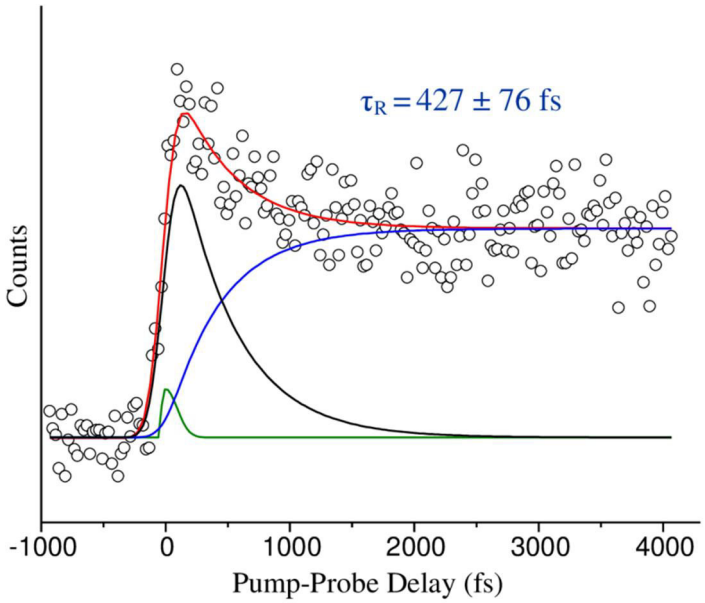

Figure 3.8 The delay trace associated with the TR-IY of the indolyl radical (mass/z = 116 in Figure 3.6) is shown with the overall best-fit trendline (red) and each individual component. Only two of three time constants from the parent ion are needed: One corresponding to $^1L_a \rightarrow {}^1L_b/{}^1\pi\sigma^*$ internal conversion (green) and the other to relaxation on the $^1\pi\sigma^*$ state (black). A rise time of 427 ± 76 fs is extracted from the blue trace. Figure reproduced with permission from J. Chem. Phys. **141**, 044314 (2014). Copyright 2014 AIP Publishing LLC.

CHAPTER 4

PUMPING INDOLE IN THE 249-282 NM RANGE

The following chapter is adapted with permission from T. J. Godfrey, H. Yu, M. S. Biddle, and S. Ullrich, *Phys. Chem. Chem. Phys.*, 2015, **17**, 25197.

A complementary TR-IY scan under otherwise identical experimental conditions was conducted for all of the investigations discussed in detail below. In each case, the resulting mass spectra confirmed the dominating presence of indole in the gas phase. With the chosen pump and probe powers, a negligible amount of fragmentation (*i.e.*, anything other than H-atom dissociation from the N-H moiety) is observed in all cases and does not require consideration in our analyses. As an additional note, the parent ion signal in the TR-IY scans were well described with the same Gaussian convoluted exponential decay functions and time constants (within the given errors) as the TR-PES data presented below.

Time-Resolved Kinetic Energy Release

The steady-state H-atom kinetic energy spectra of indole photodissociated at 241, 250, 260, and 273 nm are discussed here. In each case, the probe wavelength is centered at 243.15 nm. The Gaussian cross-correlations, as measured within the spectrometer, are as follows: 248 ± 7, 223 ± 9, 218 ± 9, and 181 ± 8 fs, respectively. As mentioned in Chapter 1, H-atoms deriving from direct dissociation along the $^1\pi\sigma^*$ state are easily distinguished from H-atoms produced via statistical unimolecular decay on S_0 based on their kinetic energies. To demonstrate this, H-atom kinetic energy spectra recorded at 273 and 250 nm are displayed in Figure 4.1(a) and Figure 4.1(b), respectively. Contributions from statistical decay are fitted with a Boltzmann distribution

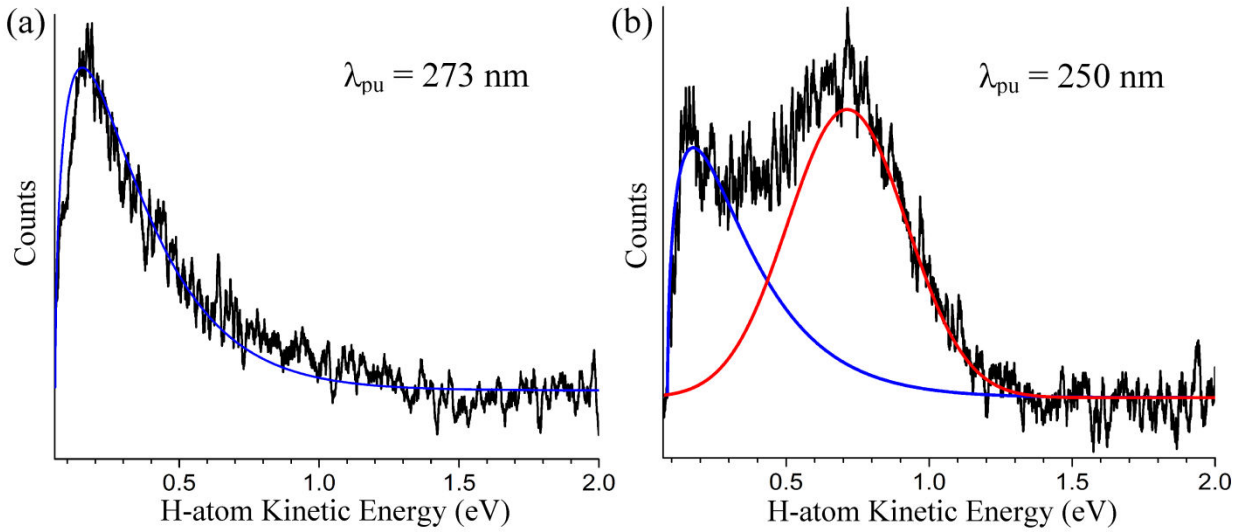

Figure 4.1 The steady-state H-atom kinetic energy spectra of indole photodissociated at (a) 273 nm and (b) 250 nm are presented here to highlight the presence of a high-energy H-atom distribution at pump wavelengths shorter than ~263 nm. The low-energy signal in both figures is fitted with a statistical function (shown in blue) while the high-energy H-atom distribution, associated with direct N-H dissociation along the $^1\pi\sigma^*$ state, is fitted with a Gaussian function (shown in red). Figure reproduced with permission from *Phys. Chem. Chem. Phys*, 2015, **17**, 25197. Copyright 2015 the Owner Societies.

(blue) whereas direct dissociation products are described by a Gaussian (red). Clearly, a bimodal distribution is observed at 250 nm but the higher kinetic energy peak is noticeably absent at 273 nm; indications of high-energy H-atom signal become visible in the low- to mid-260 nm range but signal levels are insufficient for further analysis. All of the recorded spectra discussed here resemble low-resolution versions of those attained by Ashfold and co-workers[47] and reproduce their reported onset for direct H-atom elimination. In reference to our discussion in the following section, we briefly note that H-atom detection experiments do not exclude relaxation to S_0 via the $^1\pi\sigma^*$ state below this onset. In general, our H-atom kinetic energy spectra support earlier high resolution work[47] but do not contribute any additional spectroscopic information. Therefore, the following discussion focuses on the dynamics aspect of direct N-H photodissociation at 241, 250, and 260 nm. Integration over the high-energy H-atom signal in our TR-KER spectra yields

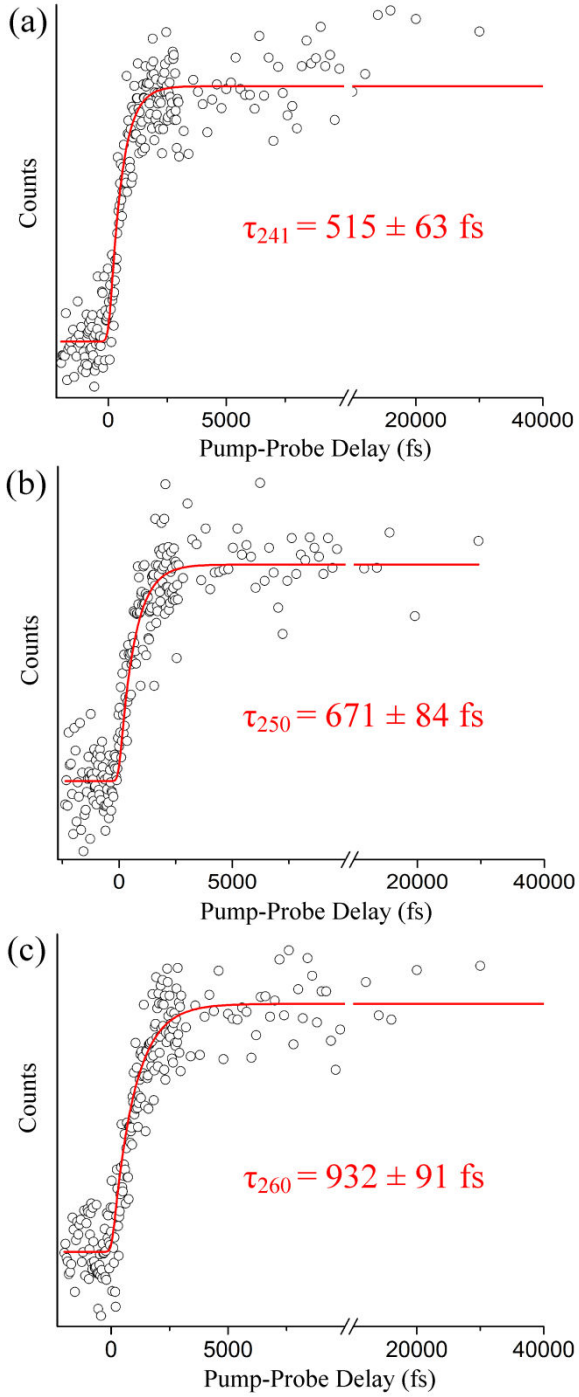

Figure 4.2 Delay traces associated with the high-energy H-atom distributions are shown here for pump wavelengths centered at (a) 241 nm, (b) 250 nm, and (c) 260 nm. A clear increasing trend in photoproduct rise time is visible as the pump wavelength increases. Figure reproduced with permission from *Phys. Chem. Chem. Phys*, 2015, **17**, 25197. Copyright 2015 the Owner Societies.

the delay traces depicted in Figure 4.2, which are then fitted with a Gaussian convoluted single-step function to extract photoproduct appearance times.

As shown in Figure 4.2(a), a high-energy H-atom rise time of τ_{241} = 515 ± 63 fs is obtained following excitation at 241 nm. When the excitation wavelength increases to 250 nm (see Figure 4.2(b)), the rise time associated with the high-energy H-atoms increases to τ_{250} = 671 ± 84 fs. The trend continues when the wavelength is again raised to 260 nm, producing a rise time of τ_{260} = 932 ± 91 fs as presented in Figure 4.2(c). While the measured time constants correspond to the appearance of the H-atom photoproduct, it may be regarded as an indirect measurement of relaxation along the $^1\pi\sigma^*$ state. As such, the increase in rise time may be suggestive of a barrier existing along the $^1\pi\sigma^*$ potential energy profile, as predicted by Townsend and co-workers[7] and Sobolewski and Domcke,[10,16] which is approached at the longer excitation wavelengths. Although both authors agree a barrier may exist, the height of the barrier is still unsure (ranging from 0.1 eV to approximately 0.5 eV). This picture is revisited in the next section when TR-KER and TR-PES results are compared and an alternative explanation is offered.

Time-Resolved Photoelectron Spectroscopy

The photoelectron spectra presented here are taken at pump wavelengths of 241, 250, 260, 270, 273, and 282 nm. A 294 nm probe is applied in all cases. A short-range scan with pump-probe delays extending ~4000 fs beyond time-zero with a step size of 25 fs is reported here at all pump wavelengths. A second set of experiments with pump-probe delays expanding beyond 100 ps with larger, unequal step sizes are also discussed at all pump wavelengths below 282 nm. The Gaussian cross-correlations for the short-range scans are 208 ± 8, 184 ± 5, 237 ± 9, 214 ± 6, 209 ± 9, and 172 ± 8 fs, respectively. Likewise, the Gaussian cross-correlations for the

long-range scans are 228 ± 7, 174 ± 6, 237 ± 9, 214 ± 6, and 201 ± 5, respectively. Each short-range scan is deconvoluted into its individual contributions (channels) using a custom LabVIEW program based on a Levenberg-Marquardt optimization algorithm, which simultaneously fits spectra and associated decay dynamics along the energy and pump-probe delay axes. The number of channels assigned in each analysis is based on the necessity to accurately fit the data (*i.e.*, the lowest number of channels where any residual signal is negligible and random noise). The results are then interpreted by considering ionization correlations (discussed in more detail shortly) and comparing our experimental outcomes to the numerous theoretical investigations.[7,10,12-16,32] Three excited-state channels are needed to accurately fit the data attained at pump wavelengths centered around 241, 250, and 260 nm. At 270 and 273 nm, only two excited-state channels are required to accurately fit the results and only one at 282 nm. It is assumed in all cases at or shorter than 273 nm that the ^1L_a state is excited almost exclusively, thus a rise time of zero femtoseconds is fixed for the ^1L_a-state contribution throughout our analysis. To account for sequential dynamics from the ^1L_a state, rise times for the ^1L_b-state and $^1\pi\sigma^*$-state contributions, when applicable, remain open during the fitting process and consistently converge to values similar to the ^1L_a-state decay times. Excitation at 282 nm corresponds to direct excitation of the ^1L_b state (*i.e.*, energetically below the ^1L_a onset), hence the rise time associated with the ^1L_b state is fixed at zero femtoseconds in this case.

Similarly, the long-range scans acquired at pump wavelengths of 241, 250, and 260 nm are accurately fitted with a Gaussian convoluted triple exponential decay function, and those at 270 and 273 nm with a Gaussian convoluted double exponential decay function. Again, exponential rises account for the sequential dynamics. The long-range scans are necessary to accurately extract time constants associated with the long-lived ^1L_b channels.

In all cases, an additional channel with a negative decay constant is introduced to account for minor probe-pump signal; however, these channels are unrelated to the excited-state dynamics of interest and not discussed further.

The color maps depicted in Figure 4.3 represent the extracted channels at pump wavelengths of 241, 250, 260, 270, and 273 nm as a function of pump-probe delay and electron binding energy. Due to differing dynamics and for clarification, the color maps corresponding to 282 nm excitation are shown separately in Figure 4.4 The electron binding energy is readily calculated by subtracting the measured photoelectron kinetic energies from the total pump and probe photon energies. In all cases, it is assumed only one photon from each beam is absorbed by the molecule, which can be justified for the laser powers and focusing conditions applied here. The first vertical ionization potential (labeled IP1) for indole is marked by the yellow-dashed line at 7.90 eV[43-45] in the second, third, and fourth columns of Figure 4.3 and is used to help identify the electronically excited states. The first column in Figure 4.3 displays the raw TR-PES signal for comparison to the individual contributions from each excited state. The second column consists of the channels associated with ^1L_a-state deactivation to the ^1L_b state and, at shorter wavelengths, also the $^1\pi\sigma^*$ state. As mentioned in an earlier investigation (see Chapter 3),[63] the $^1L_a \rightarrow {}^1L_b$ and $^1L_a \rightarrow {}^1\pi\sigma^*$ competing transitions occur simultaneously and are, in general, not discernable from one another due to spectral overlap in addition to similar ultrafast decay dynamics. Therefore, only a single time constant is assigned to the depopulation of the initially excited ^1L_a state. The third column in Figure 4.3 presents a relatively long-lived signal associated with ^1L_b-state relaxation to the S_0 state. Column 4 encompasses the channels associated with deactivation along the $^1\pi\sigma^*$ state, which is observed at pump wavelengths of 241, 250, and 260 nm but not at 270 or 273 nm.

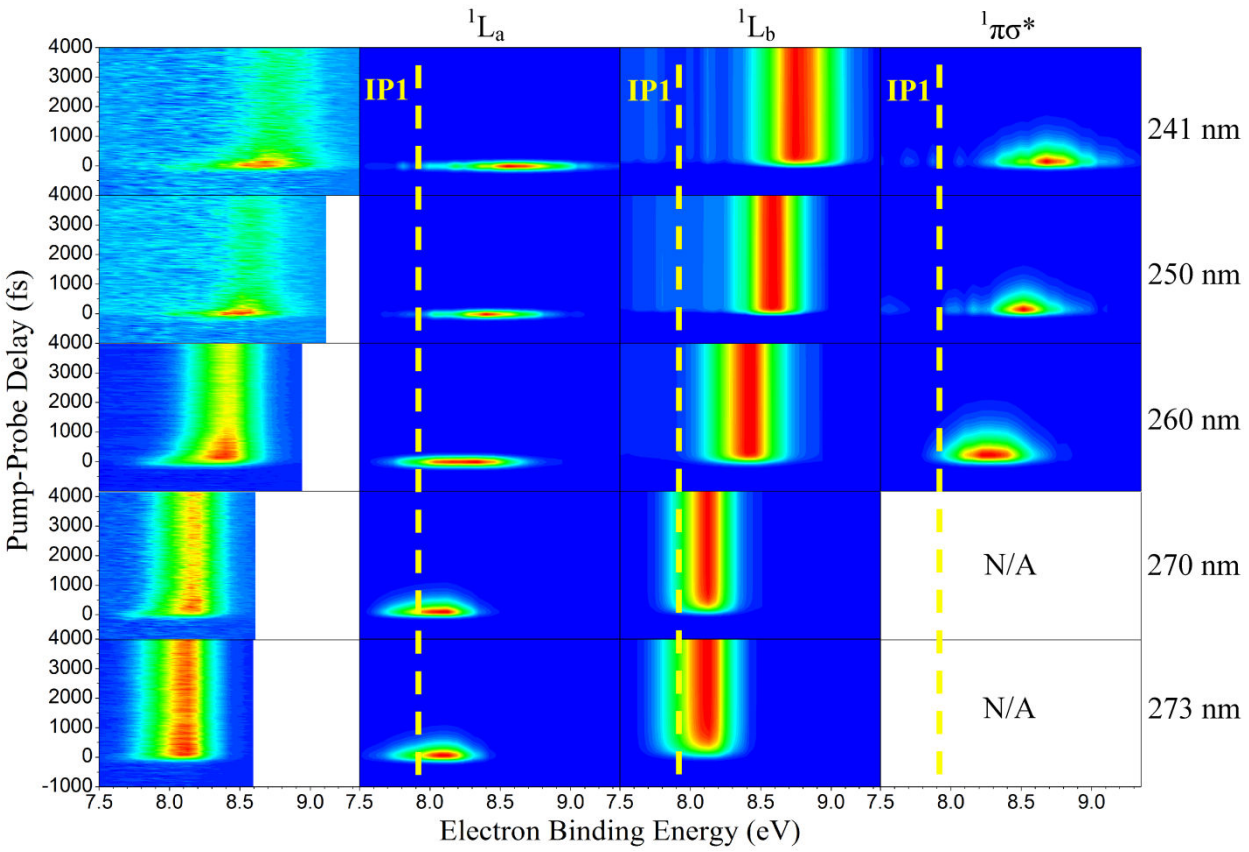

Figure 4.3 Color maps are presented here for each ^1L_a-state (column 2), ^1L_b-state (column 3), and $^1\pi\sigma^*$-state (column 4) contribution obtained through the global analysis of the raw TR-PES data (column 1) acquired at pump wavelengths of (from top to bottom) 241, 250, 260, 270, and 273 nm. The measured photoelectron kinetic energies are transformed to electron binding energies for comparison to the known indole ionization potentials. The yellow-dashed lines mark the first indole vertical ionization potential at 7.90 eV. Figure reproduced with permission from *Phys. Chem. Chem. Phys*, 2015, **17**, 25197. Copyright 2015 the Owner Societies.

Figure 4.4 is structured similarly with the raw TR-PES signal presented in column 1 and contributing channels in columns 2 and 3. IP1 is again marked with a yellow-dashed line in column 3. As mentioned earlier, excitation at 282 nm directly excites the ^1L_b state; however, two channels are needed to accurately fit the data set: one accounting for ^1L_b-state activity (excited-state channel) and another accounting for a Gaussian-shaped contribution. We will elaborate on the assignments by examining the indole ionization correlations in the subsequent paragraphs.

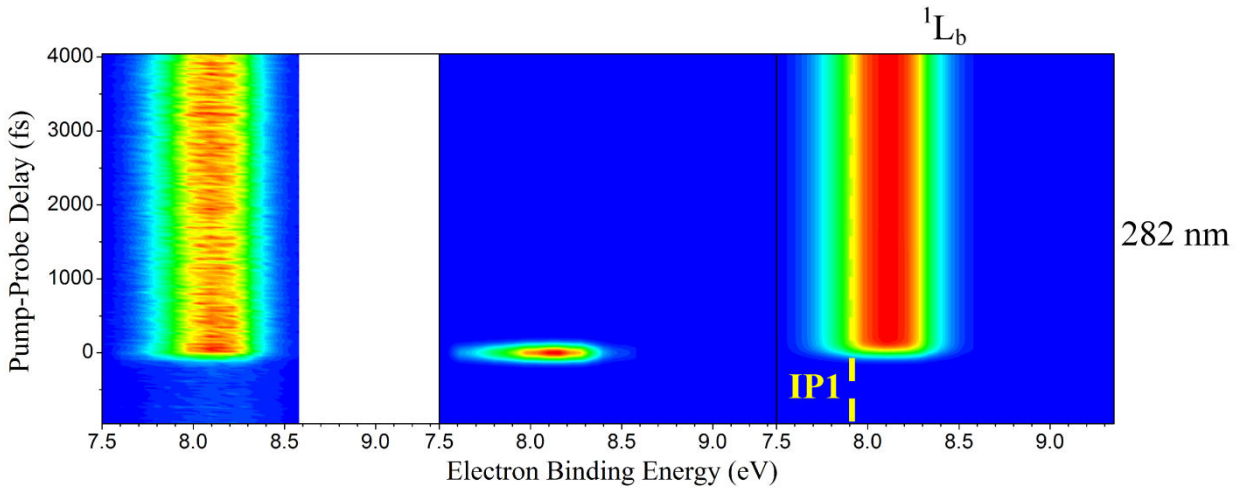

Figure 4.4 Color maps of the raw TR-PES data set (column 1) and individual channels (columns 2 and 3) are shown for indole photoexcited at 282 nm. Measured photoelectron kinetic energies are transformed to electron binding energies for comparison to the known indole ionization potentials. The yellow-dashed line marks the first indole ionization potential at 7.90 eV. Figure reproduced with permission from *Phys. Chem. Chem. Phys*, 2015, **17**, 25197. Copyright 2015 the Owner Societies.

The following discussion commences by examining indole ionization correlations. Because the ^1L_a state is populated from the highest occupied molecular orbital (HOMO),[5,7,12,14,16] it is supposed that this state preferentially ionizes into the D_0 state, which is associated with IP1 at 7.90 eV. In a very simple picture a $\Delta v = 0$ propensity is assumed, where v is a generalized quantum number and not mode specific, and any vibrational excitation in the ^1L_a state is transitioned to the ionic state. Therefore, shifts relative to the ionization potentials, in this case IP1, on an electron binding energy graph are expected. For example, the indole molecule is at first excited approximately 0.60 eV above the ^1L_a-state origin (273 nm) following absorption of a 241 nm photon. Assuming a $\Delta v = 0$ propensity, we predict the maximum signal originating from the ^1L_a state to be positioned near 8.50 eV (*i.e.*, 0.60 eV higher in binding energy than IP1), which is observed in our experimental work (see Figure 4.3). Likewise, the ^1L_a-state signal should exhibit shifts from approximately 0.42 to 0 eV when pump wavelengths in the 250 to 273 nm region are employed. This expected and observed trend further ascertains our classification

of these signal contributions as originating from the ^1L_a state and confirms an $^1L_a \rightarrow D_0$ (IP1) ionization correlation.

As mentioned by Townsend *et al.*,[7] it may be assumed (based on several band decomposition studies[64-68]) that, almost exclusively, the ^1L_a state is excited in the pumping process, especially at the excitation wavelengths well above the ^1L_a-state onset of 4.54 eV. As such, population of the ^1L_b state may solely be the result of relaxation from the ^1L_a state. Nevertheless, a similar analysis of the photoelectron spectra is implemented to study signals associated with the ^1L_b state. Based on the orbital calculations of Townsend *et al.*,[7] the ^1L_b-state transition is expected to predominantly originate from the HOMO-1 and would therefore preferentially ionize into the D_1 state, which should correspond with indole's second vertical ionization potential (IP2) of 8.35 eV.[43-45] With the ^1L_b-state origin taken to be at 283.8 nm,[69] vibrational shifts in the approximate range of 0.77 to 0.03 eV above IP2 would be expected as the pump wavelength increases from 241 nm to 282 nm. As shown in Figures 4.3 and 4.4, a general "shifting" trend is observed; however, the maximum signal peaks at all excitation wavelengths are consistently located below these predictions. Most notably for excitation at long wavelengths, the ^1L_b photoelectron signals fall below IP2. Townsend *et al.* observed a similar discrepancy in their analysis—an outcome they relate to the transmission efficiency of their spectrometer. Instead we challenge the proposed $^1L_b \rightarrow D_1$ (IP2) ionization correlation. According to Platt's notation,[11] the ^1L_b transition originates from LUMO+1 $\leftarrow$ HOMO and LUMO $\leftarrow$ HOMO-1 excitations. Close inspection of the orbital representations associated with the HOMO and HOMO-1 reveals stark differences throughout the literature and coefficients describing the relative contributions of orbital promotions are also inconsistent.[5,7,12,14,16,70] Given that theoretical descriptions are presently inconclusive, we propose an $^1L_b \rightarrow D_0$ (IP1) ionization correlation

based on our experimental observations. For instance, assuming ionization into the D_0 (IP1) state, vibrational shifts in the approximate range of 0.77 to 0.03 eV above IP1 would be expected as the pump wavelength increases from 241 to 282 nm. This is observed in all cases (see Figures 4.3 and 4.4). Furthermore, the 282 nm TR-PES spectrum in Figure 4.4 clearly demonstrates ionization of ^1L_b into D_0 (IP1) and further substantiates our proposal. A similar disparity exists for the $^1\pi\sigma^*$-state ionization correlations and, following the same arguments, we also propose preferential ionization into D_0 (IP1). In any case, assignment of the $^1\pi\sigma^*$ channel is unambiguously supported by the above TR-KER measurements.

As shown in Figure 4.4, two pump-probe channels are needed to accurately fit the raw data set acquired at 282 nm. While the photoelectron spectra of both channels (columns 2 and 3) are very similar (*i.e.*, they fall within the same electron binding energy range), a single exponential decay function would be insufficient to adequately describe the dynamics. With the excitation onset of the ^1L_a state located at 273 nm, it is assumed at 282 nm that we are pumping directly into the ^1L_b state, and we associate the long-lived channel (column 3) with ^1L_b-state activity because this contribution is highly consistent with the ^1L_b-state channels of Figure 4.3 and is congruous with our proposed $^1L_b \rightarrow D_0$ (IP1) ionization correlation. Because 282 nm is slightly above the ^1L_b-state onset, it is possible that the signal in column 2 corresponds to motion from the Franck-Condon region toward the ^1L_b minimum. Another likely cause is nonresonant ionization or out-of-resonance adiabatic excitation, which are not related to the excited-state dynamics of interest. A similar effect as these latter contributions has been observed by Longarte *et al.* in naphthalene and the related tryptophan molecule.[71,72]

We now focus our discussion on the associated time traces. The raw data sets, overall fits, and separate channel contributions associated with the short-range experiments administered at

241, 250, 260, 270, and 273 nm are displayed in Figure 4.5. Results at 282 nm are shown in Figure 4.6. We designate the green delay traces to relaxation originating from the ^1L_a state. All purple and black delay traces are attributed to relaxation along the ^1L_b state and $^1\pi\sigma^*$ state, respectively. The black-dashed lines represent the aforementioned probe-pump contributions. In Figure 4.6, the blue-dashed line depicts the Gaussian-shaped contribution mentioned earlier.

Our discussion will begin with the results obtained following excitation at 241 nm. Three time constants related to excited-state dynamics are needed to properly fit the obtained data set. The green delay trace furnishes the leading contribution to the overall signal and carries a relaxation time on an ultrafast timescale ($\tau_1 < 100$ fs). A second time constant, $\tau_2 = 436 \pm 157$ fs, is also extracted from the fitting process and is denoted by the black delay trace. This lifetime, although still extremely fast, is notably longer than the first time constant. The third and final time constant, $\tau_3 = 371 \pm 85$ ps, is from the long-lived contribution represented by the purple delay trace. These results are in strong agreement with the TR-IY studies conducted by Longarte *et al.*[49] at a pump wavelength of 243 nm. Longarte *et al.* report time constants of 22 ± 9 fs (similar to our τ_1), 435 ± 125 fs (in agreement with our τ_2), and 315 ± 50 ps (in agreement with our τ_3). It should be noted, however, that Longarte *et al.* employ a 1305 nm multiphoton probe, which, in principle, could produce contrasting dynamics if intermediate resonances are hit during the ionization process.

Because we associate τ_2 with relaxation along the $^1\pi\sigma^*$ state, this time constant can be compared to our independent H-atom TR-KER results discussed in the previous section. The time constants are in agreement within the reported error, although the TR-KER value is somewhat longer. While it is certainly possible that this difference corresponds to the additional time required for the formation of the fully separated photoproduct, another possible explanation

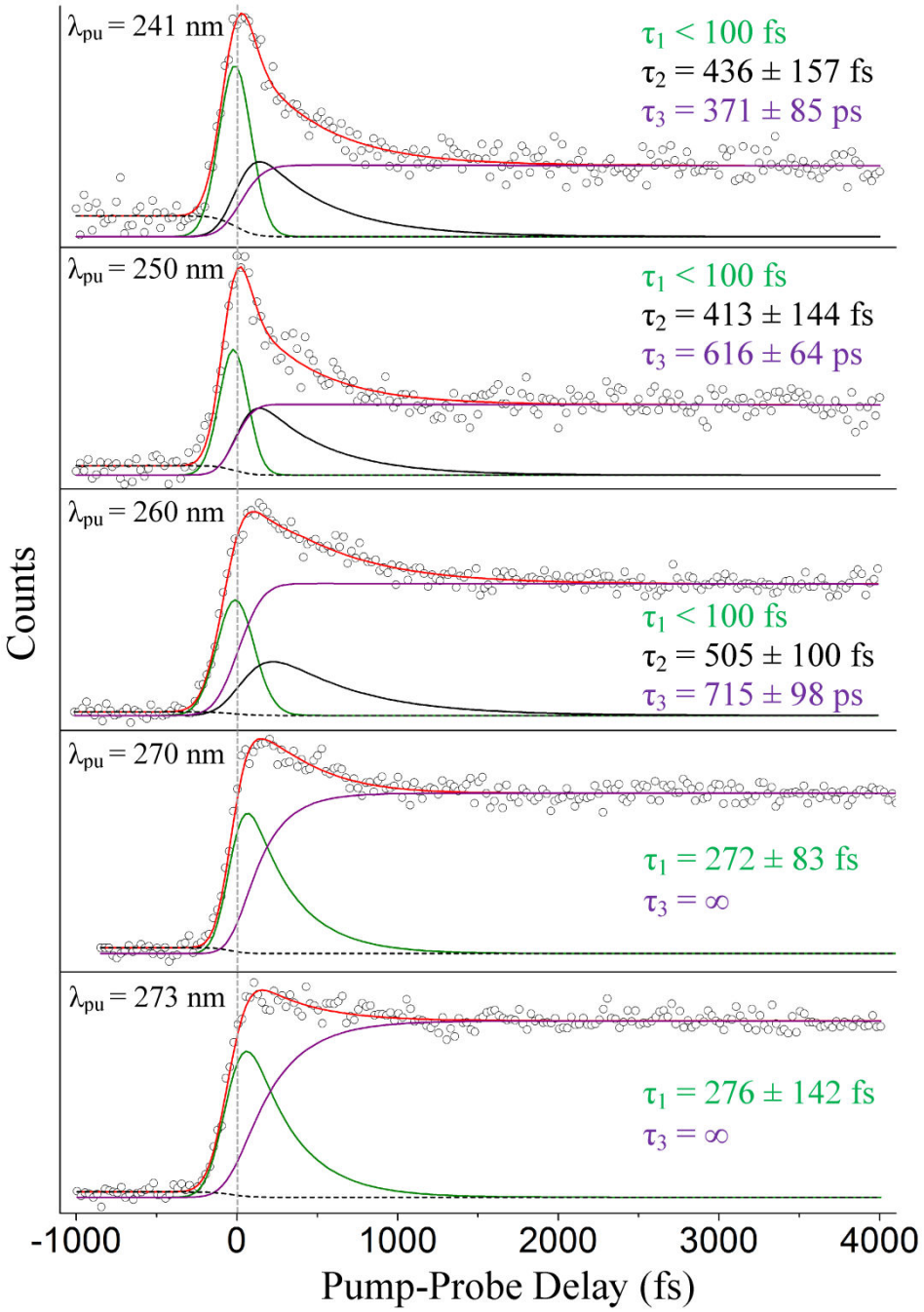

Figure 4.5 Short-range TR-PES signal (○), fits (red), and individual contributions (^1L_a – green, $^1\pi\sigma^*$ – black, ^1L_b – purple, and probe-pump signal – black-dashed) integrated over all photoelectron kinetic energies are shown at various pump wavelengths: (from top to bottom) 241, 250, 260, 270, and 273 nm. Relaxation times associated with each channel (^1L_a – τ_1, $^1\pi\sigma^*$ – τ_2, ^1L_b – τ_3) are also displayed in their respective graphs. The zero position is marked by the gray-dashed vertical line. Figure reproduced with permission from *Phys. Chem. Chem. Phys*, 2015, **17**, 25197. Copyright 2015 the Owner Societies.

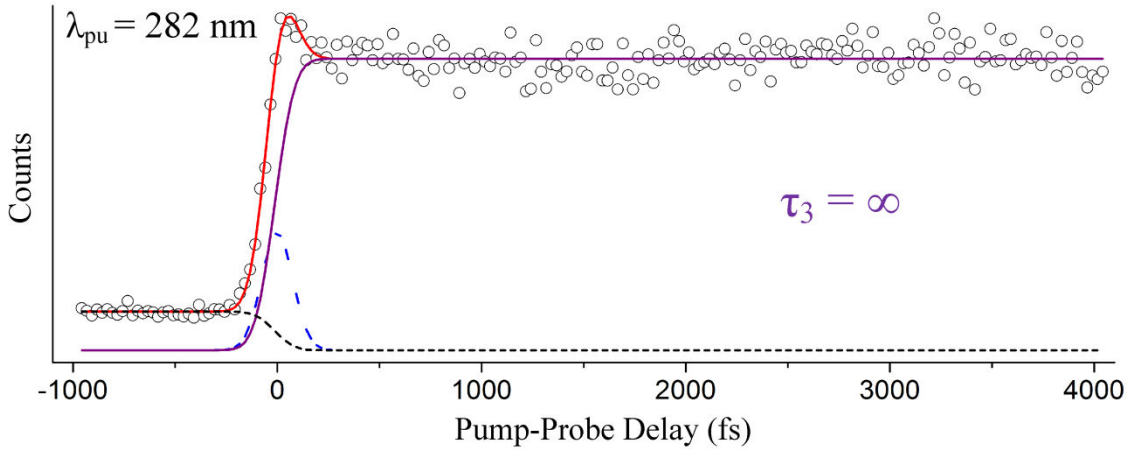

Figure 4.6 Short-range TR-PES signal (○), fit (red), and individual contributions (^1L_b – purple, nonresonant activity – blue-dashed, and probe-pump signal – black-dashed) integrated over all photoelectron kinetic energies are shown following photoexcitation at 282 nm. Figure reproduced with permission from *Phys. Chem. Chem. Phys*, 2015, **17**, 25197. Copyright 2015 the Owner Societies.

is discussed below. Likewise, the separate long-range TR-PES scan from which τ_3 derives is described very well with these same time constants (see Figure 4.7).

At a pump wavelength centered around 250 nm, three time constants associated with excited-state relaxation dynamics are gleaned: $\tau_1 < 100$ fs, $\tau_2 = 413 \pm 144$ fs, and $\tau_3 = 616 \pm 64$ ps. Increasing the pump wavelength from 241 nm to 250 nm did not reveal any pronounced changes in τ_1 or the lifetime associated with $^1\pi\sigma^*$-state activity (τ_2); however, a significant increase in decay time is detected for the ^1L_b-state (τ_3) signal, which is nearly double that at 241 nm. Our result for τ_1 is consistent with that obtained by Townsend *et al.*,[7] who report a value of <100 fs at a pump wavelength of 249 nm, and Longarte *et al.*, who report 22 ± 9 fs at a pump wavelength of 248 nm. However, a noticeable difference between our result for τ_2 and Townsend *et al.* is now made manifest. At essentially the same wavelengths as those applied here, Townsend *et al.* establish a lifetime of approximately 700 fs for the $^1\pi\sigma^*$ state, which is much different than our $\tau_2 = 413 \pm 144$ fs. Our results are more comparable to those reported by Longarte *et al.*, who report a $^1\pi\sigma^*$-state lifetime of 460 ± 145 fs. Unlike the case at 241 nm, τ_2

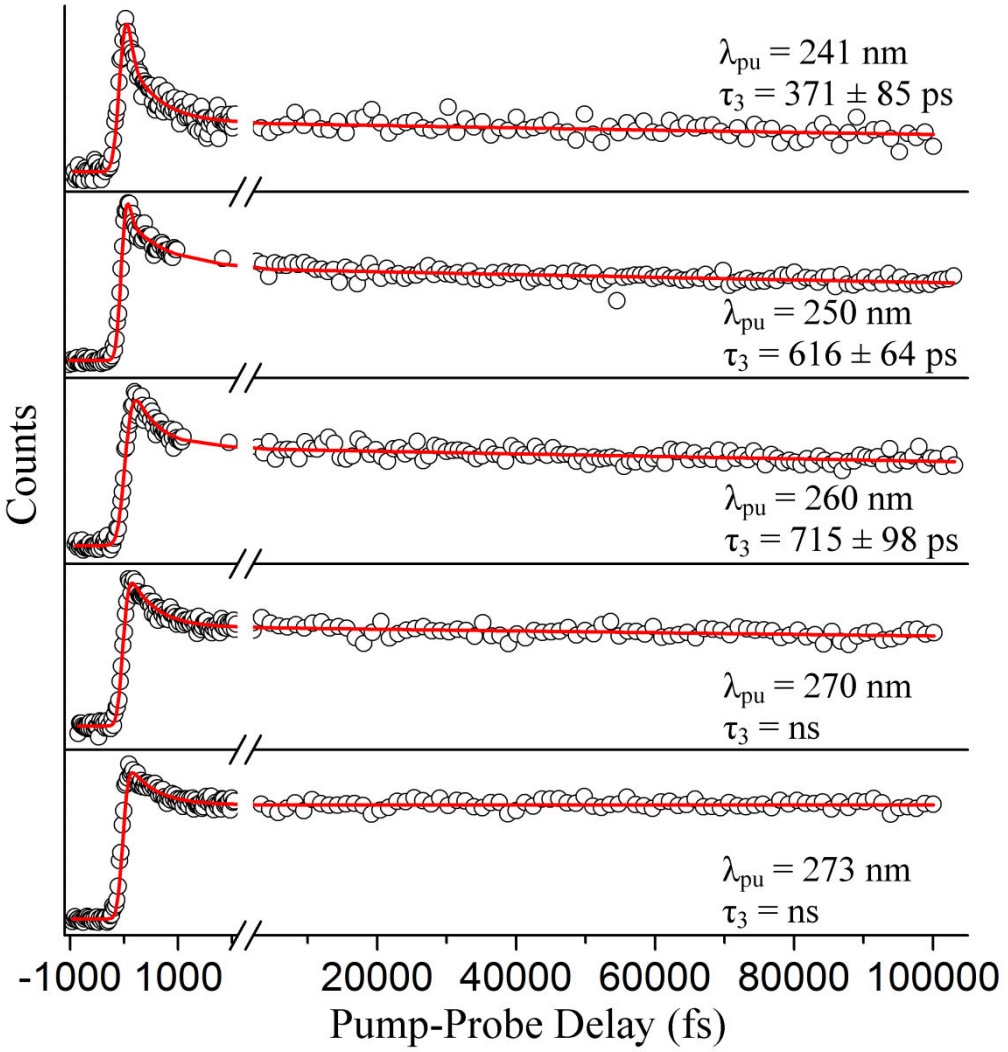

Figure 4.7 TR-PES signal (○) for the long-range scans and fits (red) integrated over all photoelectron kinetic energies are shown to complement the short-range scans displayed in Figure 4.5. The pump wavelengths here (from top to bottom) are 241, 250, 260, 270, and 273 nm. Relaxation times associated with the $^1L_b \rightarrow S_0$ transition (τ_3) are also displayed in their respective graphs. Figure reproduced with permission from *Phys. Chem. Chem. Phys*, 2015, **17**, 25197. Copyright 2015 the Owner Societies.

extracted via TR-PES does not corroborate the rise time τ_{250} = 671 ± 84 fs from the previously discussed TR-KER experiments in the previous section. We believe the reason for this difference can be linked to the loss of the ionization window between the downward curving $^1\pi\sigma^*$-state potential energy profile[7,10,16] and the upward curving ionic-state potential as the N-H bond length increases,[73] an issue that has previously been raised in the literature for the case of adenine.[74]

Indirect measurements such as TR-KER are unaffected by this issue since the probe process relies on the photoionization of H-atoms. It is therefore our conclusion that the TR-KER results presented in the previous section are more representative of the actual relaxation times associated with $^1\pi\sigma^*$ decay. Once the $^1\pi\sigma^*/S_0$ conical intersection has been passed, dissociation occurs quickly on the repulsive potential energy curve. Furthermore, the large discrepancy between TR-KER and TR-PES time constants suggests that a significant portion of the dynamics occur at extended N-H distances, most likely in the vicinity of the conical intersection, where they are inaccessible to direct photoionization at the utilized probe wavelength.

It should also be noted that there is a substantial disagreement between our τ_3 and the long-lived component measured by Townsend *et al.*[7] These authors report a long-lived component with an associated lifetime of 350 ps, nearly half our value, following excitation at 249 nm. One possible reason for this disparity is the maximum scanning range beyond time-zero. In principle, the extracted time constants should be independent of the selected scanning range, but it is our experience that values can vary significantly due to the presence of noise in real data sets. Townsend *et al.*'s scan range extends to approximately 50 ps; whereas, this investigation scans slightly over double that range to extract the long-lived contribution to the signal (see Figure 4.7). The work of Longarte *et al.*[49] reports a value in the picosecond range; however, it is unclear where exactly in the picosecond range their value is located. It should also be noted that none of the studies (here or in the literature) observe the long-lived signal levels decaying back to a zero baseline. Further insight regarding this disparity may be gleaned by continuing this discussion following the reports at the remaining excitation wavelengths. As such, we will return to this comparison shortly.

Following excitation at 260 nm, time constants of $\tau_1 < 100$ fs, $\tau_2 = 505 \pm 100$ fs, and $\tau_3 = 715 \pm 98$ ps are acquired. Again, no considerable change in τ_1 or τ_2 is observed in this case, but in comparison to the previous section, the difference between the TR-KER and TR-PES $^1\pi\sigma^*$ time constants increases further. Longarte *et al.*[49] report time constants of 22 ± 9 fs and 370 ± 110 fs for activity correlated with ^1L_a-state and $^1\pi\sigma^*$-state deactivation, respectively, following excitation at the same pump wavelength. However, another dissimilarity presents itself between our $\tau_3 = 715 \pm 98$ ps and the work of Longarte *et al.* Scanning nearly 140 ps beyond time-zero, their work reports a lifetime of 7 ± 2 ns associated with ^1L_b-state relaxation. To address this discrepancy, a separate scan (not presented here) extending beyond 200 ps was conducted, and the extracted decay constants verify the values reported here. The reason for this difference is not clear but, as mentioned earlier, could be related to the scanning range or the multiphoton nature of the ionization process employed by Longarte *et al*. Further picosecond or nanosecond time-resolved studies may aspire to investigate the time constants associated with ^1L_b-state relaxation following excitation at 260 nm to verify these claims.

Following excitation at 270 nm, only two time constants are needed to accurately fit the data set: $\tau_1 = 272 \pm 83$ fs and $\tau_3 =$ ns. Likewise at 273 nm, two time constants associated with excited-state dynamics are extracted: $\tau_1 = 276 \pm 142$ fs and $\tau_3 =$ ns. To our knowledge, no prior work associates similar time constants to ^1L_a-state relaxation for excitation close to the origin. However, the aforementioned discussion regarding ionization correlations strongly supports this assignment. Similar to our previous scans, the separate long-range scan is also accurately fitted with these short-range time constants (see Figure 4.7). These results challenge the assignment of an ultrafast time constant (*i.e.*, <100 fs) to ^1L_a-state relaxation by Townsend *et al.* and Longarte *et al.* For further discussion, we refer to the potential energy profiles calculated along ring

deformation coordinates by Giussani *et al.*[14] Their calculation positions the $^1L_a/^1L_b$ conical intersection in very close vicinity to the ^1L_a-state minimum which, at first sight, seems to strongly support an ultrafast transition. However, Giussani *et al.* report theoretical ^1L_a- and ^1L_b-state minima that are lower than the experimental onsets according to Refs. 30, 31, and 69 by approximately 0.14 and 0.26 eV, respectively. If these same curves are shifted upward to the known experimental values, the separation between the conical intersection and the ^1L_a-state minimum increases and our slightly longer τ_1 constants are certainly not unreasonable.

As far as this experimental work is concerned, there is no apparent contribution originating from the $^1\pi\sigma^*$ state at 270 and 273 nm. The fact that a third excited-state relaxation channel is not necessary to accurately fit the short-range scans presented in Figure 4.5 or the long-range scans in Figure 4.7 supports this claim. As mentioned earlier, the number of channels chosen at each pump wavelength is based on the necessity to obtain an accurate fit. For instance, when the data acquired at 241, 250, and 260 nm is fitted with only two excited-state channels, the residual signal clearly displays unaccounted for contributions to the overall signal, often in the ultrafast region of the spectrum. This is not the case at 270 and 273 nm where both data sets are accurately described using only two excited-state channels. To visualize these effects, Figure 4.8 selectively displays the residuals for the 260 and 270 nm TR-PES spectra when fit with only two pump-probe channels. We also note, that forcing an additional, unnecessary channel into the 270 and 273 nm fits leads to a spectral deconvolution into features that are incompatible with our general analysis (*i.e.*, ionization correlations and vibrational shifts are inexplicable).

The ultrafast electron diffraction results reported by Zewail and co-workers[75] bolster this interpretation as well. In their experimental work, the authors conclude that the $^1\pi\sigma^*$ state does not play a significant role in indole relaxation dynamics following excitation at 267 nm. This is

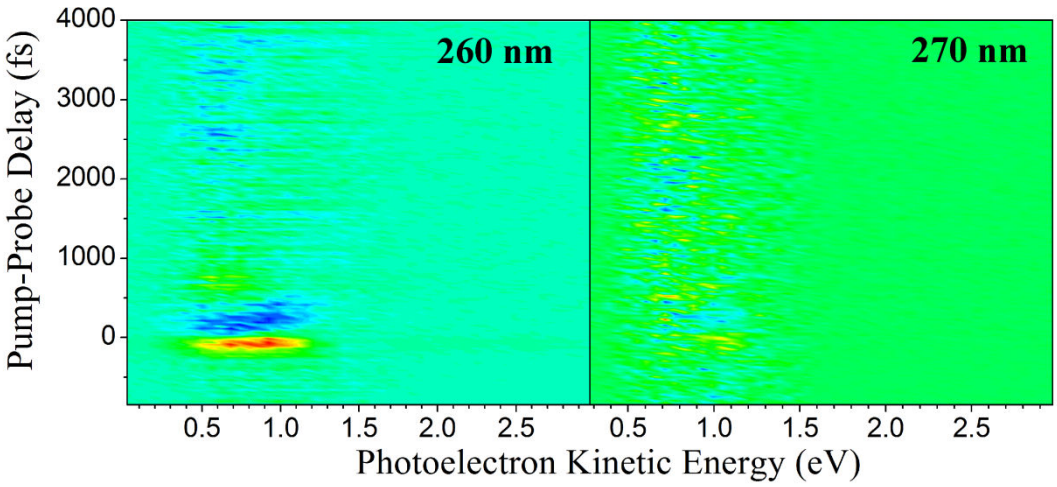

Figure 4.8 When fitted with only two excited-state channels, the residual signal following excitation at 260 nm (left) clearly displays unaccounted for signal, thus requiring the inclusion of a third pump-probe channel. However, the photoelectron signal acquired at 270 nm is adequately described using only two pump-probe channels (right). Figure reproduced with permission from *Phys. Chem. Chem. Phys*, 2015, **17**, 25197. Copyright 2015 the Owner Societies.

in direct contrast with Townsend *et al.*,[7] who compare their results taken at 249 nm, where the $^1\pi\sigma^*$ state is actively involved in the relaxation process, and 273 nm to arrive at the conclusion that the $^1\pi\sigma^*$ state is participating in the relaxation process at 273 nm. The previously discussed TR-KER results provide no evidence for $^1\pi\sigma^*$-state activity at 273 nm either; however, the TR-KER measurements only identify the onset of H-atom dissociation from the N-H moiety along the $^1\pi\sigma^*$ state, which may differ from the onset of $^1\pi\sigma^* \rightarrow S_0$ relaxation. We do acknowledge that, in principle, it is possible for the $^1\pi\sigma^*$ state to actively participate in the relaxation process at these longer wavelengths without breaking the N-H bond, but there is no experimental evidence in this current study to suggest such an involvement following excitation at 270 and 273 nm.

Following excitation at 282 nm, the inclusion of a $\tau_3 = \infty$ and an approximately 0 fs component (Gaussian shown as the blue-dashed line in Figure 4.6) is necessary to accurately fit the data set. The channel associated with τ_3 essentially resembles a step function. τ_3 is highly consistent with the results reported by Longarte *et al.*[49] following excitation at 283 nm. However,

these authors do not observe the 0 fs relaxation time that we associate with nonresonant signal nor do they see signs of such a process when pumping at 278 nm. Instead, Longarte *et al.*'s TR-IY results at 278 nm contain an exponentially rising signal that they relate to an increase in the overall ionization cross-section.

We now return to the discussion regarding the ^1L_b-state relaxation times. As mentioned earlier, the extracted time constant τ_3 following excitation at 250 nm disagrees with Townsend *et al.*[7] by nearly a factor of two. Likewise, τ_3 differs quite significantly with the work of Longarte *et al.*[49] following excitation at 260 nm. Yet even with these disagreements, the nanosecond decay times associated with ^1L_b-state activity following excitation at 270 and 273 nm broadly agree with both Townsend *et al.*, who utilize a 273 nm pump, and Longarte *et al.*, who employ pump wavelengths set at 269 and 272.5 nm. However, a strict comparison to our results is not possible because neither Townsend *et al.* nor Longarte *et al.* report the ^1L_b-state decay values at these wavelengths, just orders of magnitude or an infinite decay relative to the scanned region. One possible reason, as suggested earlier, for the discrepancies at 250 and 260 nm is the difference in observed pump-probe delay ranges. We simply note the observed trend among our obtained values to bolster these results. According to our study, the ^1L_b state becomes longer lived as the excitation energy decreases—transitioning from a $\tau_3 = 371 \pm 85$ ps lifetime at 241 nm to the nanosecond relaxation time observed at 273 nm. This trend is also consistent with our previous work at 201 nm, where an ^1L_b-state lifetime of $\tau_3 = 23 \pm 5$ ps is reported.[63]

CHAPTER 5

CONCLUSIONS

The relaxation dynamics of the indole molecule have been investigated through gas-phase TR-PES, H-atom TR-KER, and TR-IY experimental techniques following excitation at 201 nm. Measurements presented throughout this work indicate involvement of the optically bright ^1L_a and ^1L_b states as well as the optically dark $^1\pi\sigma^*$ state in the indole deactivation process. It is proposed that the lifetime of the initially excited ^1B_b state (which is most likely excited at 201 nm) is negligible within our time resolution as electronically excited indole regresses to the ^1L_a state, at which point the same relaxation pathways reported at longer wavelengths are utilized: That is, $^1L_a \rightarrow {}^1L_b/{}^1\pi\sigma^*$, $^1\pi\sigma^* \rightarrow S_0$, and $^1L_b \rightarrow S_0$ transitions are observed. The associated decay constants, as obtained from a global analysis of the TR-PES experiments, are $\tau_1 < 100$ fs, $\tau_2 = 405 \pm 76$ fs, and $\tau_3 = 23 \pm 5$ ps, respectively. All three time constants are highly corroborated by TR-IY investigations ($\tau_1 < 100$ fs and $\tau_2 = 385 \pm 69$ fs with $\tau_3 = 23 \pm 5$ ps fixed), and the component linked to $^1\pi\sigma^*$-state activity is further supported by TR-KER results ($\tau_2 = 367 \pm 39$ fs). The latter assessment is feasible due to the observed bimodal H-atom distribution, where signal associated with $^1\pi\sigma^*$-mediated N-H bond fission is clearly distinguishable from H-atoms generated by way of dissociative ionization and/or statistical unimolecular decay. As confirmed by TR-IY results, this N-H bond fission is the only fragmentation process detected within the electronically excited indole molecule. Therefore, an analysis of the resulting indolyl radical yields another evaluation of $^1\pi\sigma^*$ dynamics ($\tau_2 = 427 \pm 76$ fs).

The same pump-probe spectroscopic techniques were also utilized to study the relaxation dynamics of indole at various excitation wavelengths. The first, TR-IY, revealed negligible excited-state fragmentation other than the N-H dissociation for shorter excitation wavelengths. The second, TR-KER, afforded an analysis of the bimodal, steady-state H-atom kinetic energy spectra. High kinetic energy H-atoms associated with relaxation along the $^1\pi\sigma^*$ pathway began emanating from the N-H moiety in the mid- to low-260 nm range, which is in strong agreement with the high resolution work of Ashfold *et al.*[47] The lack of high kinetic energy H-atoms at longer wavelengths than indicated implies insufficient energy to initiate H-atom dissociation. However, for pump wavelengths centered at 241, 250, and 260 nm, the $^1\pi\sigma^*$ relaxation times exhibited a distinct trend of increasing from 515 ± 63 fs to 932 ± 91 fs. This may be indicative of a potential energy barrier existing along the $^1\pi\sigma^*$ relaxation pathway as predicted by *ab initio* calculations,[7,10] but an alternative explanation is proposed below.

These results were complemented with a series of TR-PES studies at 241, 250, 260, 270, 273, and 282 nm. The ^1L_a-state contributions exhibited ultrafast decay times at the shorter wavelengths and time constants of a couple hundred femtoseconds at 270 and 273 nm. No apparent contribution from the ^1L_a state is observed when exciting just above the ^1L_b-state onset at 282 nm. Time constants extracted from the ^1L_b signal contributions exhibited a dependence on pump wavelength: increasing from 371 ± 85 ps to the nanosecond range. In agreement with the results reported by Longarte *et al.*,[49] all $^1\pi\sigma^*$-state relaxation times were ~450 fs. This result is intriguing in light of the systematic increase in lifetimes observed with TR-KER toward longer excitation wavelengths. We attribute this discrepancy to loss of the ionization window in the TR-PES measurement caused by the downward curving $^1\pi\sigma^*$ potential energy curve and the upward trend of the ionic-state potential energy profiles. Moreover, this leads to the notion that motion in

the vicinity of the $^1\pi\sigma^*/S_0$ conical intersection (at extended N-H distances) accounts for a significant portion of the relaxation dynamics.

As far as this experimental work is concerned, there is no evidence of $^1\pi\sigma^*$-state involvement in the indole relaxation process following excitation at 270 and 273 nm—in agreement with the ultrafast electron diffraction work of Zewail and co-workers.[75]

REFERENCES

[1]G. M. Roberts and V. G. Stavros, Chem. Sci. **5**, 1698 (2014).

[2]S. J. Harris, D. Murdock, Y. Zhang, T. A. A. Oliver, M. P. Grubb, A. J. Orr-Ewing, G. M. Greetham, I. P. Clark, M. Towrie, S. E. Bradforth, and M. N. R. Ashfold, Phys. Chem. Chem. Phys. **15**, 6567 (2013).

[3]Y. Zhang, T. A. A. Oliver, M. N. R. Ashfold, and S. E. Bradforth, Faraday Discuss. **157**, 141 (2012).

[4]D. Murdock, S. J. Harris, T. N. V. Karsili, G. M. Greetham, I. P. Clark, M. Towrie, A. J. Orr−Ewing, and M. N. R. Ashfold, J. Phys. Chem. Lett. **3**, 3715 (2012).

[5]T. A. A. Oliver, Y. Zhang, M. N. R. Ashfold, and S. E. Bradforth, Faraday Discuss. **150**, 439 (2011).

[6]F. F. Crim, Faraday Discuss. **157**, 9 (2012).

[7]R. Livingstone, O. Schalk, A. E. Boguslavskiy, G. R. Wu, L. T. Bergendahl, A. Stolow, M. J. Paterson, and D. Townsend, J. Chem. Phys. **135**, 194307 (2011).

[8]P. Meredith and T. Sarna, Pigm. Cell Res. **19,** 572 (2006).

[9]P. Meredith, B. J. Powell, J. Riesz, S. P. Nighswander-Rempel, M. R. Pederson, and E. G. Moore, Soft Matter **2**, 37 (2006).

[10]A. L. Sobolewski and W. Domcke, Chem. Phys. Lett. **315**, 293 (1999).

[11]J. R. Platt, J. Chem. Phys. **17**, 484 (1949).

[12]L. Serrano-Andres and B. O. Roos, J. Am. Chem. Soc. **118**, 185 (1996).

[13]A. C. Borin and L. Serrano-Andres, Chem. Phys. **262**, 253 (2000).

[14]A. Giussani, M. Merchan, D. Roca-Sanjuan, and R. Lindh, J. Chem. Theory Comput. **7**, 4088 (2011).

[15]J. Catalan, P. Perez, and A. U. Acuna, J. Mol. Struct. **142**,179 (1986).

[16]A. L. Sobolewski and W. G. Domcke, J. Phys. Chem. A **111**, 11725 (2007).

[17]A. Z. Britten and G. Lockwood, Spectrochim. Acta, Part A **32**, 1335 (1976).

[18]G. A. Bickel, D. R. Demmer, E. A. Outhouse, and S. C. Wallace, J. Chem. Phys. **91**, 6013 (1989).

[19]G. Berden, W. L. Meerts, and E. Jalviste, J. Chem. Phys. **103**, 9596 (1995).

[20]J. Kupper, D. W. Pratt, W. L. Meerts, C. Brand, J. Tatchen, and M. Schmitt, Phys. Chem. Chem. Phys. **12**, 4980 (2010).

[21]T. L. O. Barstis, L. I. Grace, T. M. Dunn, and D. M. Lubman, J. Phys. Chem. **97**, 5820 (1993).

[22]P. R. Callis, J. T. Vivian, and L. S. Slater, Chem. Phys. Lett. **244,** 53 (1995).

[23]J. Hager and S. C. Wallace, J. Phys. Chem. **87**, 2121 **(**1983).

[24]D. M. Sammeth, S. X. Yan, L. H. Spangler, and P. R. Callis, J. Phys. Chem. **94**, 7340 (1990).

[25]R. Bersohn, U. Even, and J. Jortner, J. Chem. Phys. **80**, 1050 (1984).

[26]J. R. Cable, J. Chem. Phys. **92**, 1627 (1990).

[27]J. W. Hager, D. R. Demmer, and S. C. Wallace, J. Phys. Chem. **91**, 1375 (1987).

[28]J. M. Hollas, Spectrochim. Acta **19**, 753 (1963).

[29]Y. Nibu, H. Abe, N. Mikami, and M. Ito, J. Phys. Chem. **87**, 3898 (1983).

[30]B. J. Fender, D. M. Sammeth, and P. R. Callis, Chem. Phys. Lett. **239**, 31 (1995).

[31]V. A. Povedailo and D. L. Yakovlev, J. Appl. Spectrosc. **75**, 336 (2008).

[32]C. Brand, J. Kupper, D. W. Pratt, W. L. Meerts, D. Krugler, J. Tatchen, and M. Schmitt, Phys. Chem. Chem. Phys. **12**, 4968 (2010).

[33]H. Lippert, H. H. Ritze, I. V. Hertel, and W. Radloff, Chem. Phys. Lett. **398**, 526 (2004).

[34]A. L. Sobolewski, W. Domcke, C. Dedonder-Lardeux, and C. Jouvet, Phys. Chem. Chem. Phys. **4**, 1093 (2002).

[35]A. Iqbal and V. G. Stavros, J. Phys. Chem. A **114,** 68 (2010).

[36]H. Lami, J. Chem. Phys. **67**, 3274 (1977).

[37]H. Lami, Chem. Phys. Lett. **48**, 447 (1977).

[38]N. A. Borisevich and T. F. Raichuyonok, Dokl. Phys. **52**, 405 (2007).

[39]J. Hager, M. Ivanco, M. A. Smith, and S. C. Wallace, Chem. Phys. Lett. **113**, 503 (1985).

[40]T. Vondrak, S. Sato, and K. Kimura, J. Phys. Chem. A **101**, 2384 (1997).

[41]J. E. Braun, T. L. Grebner, and H. J. Neusser, J. Phys. Chem. A **102**, 3273 (1998).

[42]M. de Groot, J. Broos, and W. J. Buma, J. Chem. Phys. **126**, 204312 (2007).

[43]L. N. Domelsmith, L. L. Munchausen, and K. N. Houk, J. Am. Chem. Soc. **99**, 4311 **(**1977).

[44]J. H. D. Eland, Int. J. Mass Spectrom. Ion Phys. **2**, 471 (1969).

[45]L. J. Dolby, G. Hanson, and T. Koenig, J. Org. Chem. **41**, 3537 (1976).

[46]M. F. Lin, C. M. Tseng, Y. T. Lee, and C. K. Ni, J. Chem. Phys. **123**, 124303 (2005).

[47]M. G. D. Nix, A. L. Devine, B. Cronin, and M. N. R. Ashfold, Phys. Chem. Chem. Phys. **8**, 2610 (2006).

[48]N. Glasser and H. Lami, J. Chem. Phys. **74**, 6526 (1981).

[49]R. Montero, A. P. Conde, V. Ovejas, F. Castano, and A. Longarte, J. Phys. Chem. A **116**, 2698 (2012).

[50]Table reproduced with permission from *Phys. Chem. Chem. Phys.*, 2015, **17**, 25197. Copyright 2015 the Owner Societies.

[51]L. P. Maguire, S. Szilagyi, and R. E. Scholten, Rev. Sci. Instrum. **75**, 3077 (2004).

[52]P. Kruit and F. H. Read, J. Phys. E: Sci. Instrum. **16**, 313 (1983).

[53]W. C. Wiley and I. H. McLaren, Rev. Sci. Instrum. **26**, 1150 (1955).

[54]N. L. Evans, H. Yu, G. M. Roberts, V. G. Stavros, and S. Ullrich, Phys. Chem. Chem. Phys. **14**, 10401 (2012).

[55]N. L. Evans and S. Ullrich, J. Phys. Chem. A **114**, 11225 (2010).

[56]D. M. P. Holland, M. A. MacDonald, M. A. Hayes, P. Baltzer, B. Wannberg, M. Lundqvist, L. Karlsson, and W. von Niessen, J. Phys. B: At. Mol. Opt. Phys. **29**, 3091 (1996).

[57]R. Locht, K. Hottmann, G. Hagenow, W. Denzer, and H. Baumgartel, Chem. Phys. Lett. **190**, 124 (1992).

[58]A. A. Sukhodola, J. Appl. Spectrosc. **77**, 802 (2011).

[59]R. Montero, A. P. Conde, V. Ovejas, R. Martinez, F. Castano, and A. Longarte, J. Chem. Phys. **135**, 054308 (2011).

[60]R. Montero, A. Longarte, A. P. Conde, C. Redondo, F. Castano, I. Gonzalez-Ramirez, A. Giussani, L. Serrano-Andres, and M. Merchan, J. Phys. Chem. A **113**, 13509 (2009).

[61]M. N. R. Ashfold, G. A. King, D. Murdock, M. G. D. Nix, T. A. A. Oliver, and A. G. Sage, Phys. Chem. Chem. Phys. **12**, 1218 (2009).

[62]NIST Mass Spec Data Center, S.E. Stein, director, "Mass Spectra" in **NIST Chemistry WebBook, NIST Standard Reference Database Number 69**, Eds. P.J. Linstrom and W.G. Mallard, National Institute of Standards and Technology, Gaithersburg MD, 20899, http://webbook.nist.gov, (retrieved March 2, 2014).

[63]T. J. Godfrey, H. Yu and S. Ullrich, J. Chem. Phys. **141**, 044314 (2014).

[64]B. Valeur and G. Weber, Photochem. Photobiol. **25**, 441 (1977).

[65]Y. Yamamoto and J. Tanaka, Bull. Chem. Soc. Jpn. **45**, 1362 (1972).

[66]M. R. Eftink, L. A. Selvidge, P. R. Callis, and A. A. Rehms, J. Phys. Chem. **94**, 3469 (1990).

[67]R. L. Rich, Y. Chen, D. Neven, M. Négrerie, F. Gai, and J. W. Petrich, J. Phys. Chem. **97**, 1781 (1993).

[68]E. Jalviste and N. Ohta, J. Chem. Phys. **121**, 4730 (2004).

[69]B. C. Dian, A. Longarte, and T. S. Zwier, J. Chem. Phys. **118**, 2696 (2003).

[70]P. R. Callis, J. Chem. Phys. **95**, 4230 (1991).

[71]R. Montero, A. P. Conde, A. Longarte, and F. Castaño, ChemPhysChem **11**, 3420 (2010).

[72]V. Ovejas, M. Fernández-Fernández, R. Montero, F. Castaño, and A. Longarte, J. Phys. Chem. Lett. **4**, 1928 (2013).

[73]J. M. Turney, personal communication.

[74]M. Barbatti and S. Ullrich, Phys. Chem. Chem. Phys. **13**, 15492 (2011).

[75]S. T. Park, A. Gahlmann, Y. He, J. S. Feenstra, and A. H. Zewail, Angew. Chem. Int. Ed. **47**, 9496 (2008).